Forty eclipsing binaries in the Small Magellanic Cloud: fundamental parameters and Cloud distance

R. W. Hilditch,[1]* I. D. Howarth[2] and T. J. Harries[3]

[1]*School of Physics and Astronomy, University of St Andrews, North Haugh, St Andrews KY16 9SS*
[2]*Department of Physics and Astronomy, University College London, Gower Street, London WC1E 6BT*
[3]*Department of Physics, University of Exeter, Stocker Road, Exeter EX4 4QL*

ABSTRACT

We have conducted a programme to determine the fundamental parameters of a substantial number of eclipsing binaries of spectral types O and B in the Small Magellanic Cloud (SMC). New spectroscopic data, obtained with the two-degree-field (2dF) multi-object spectrograph on the 3.9-m Anglo-Australian Telescope, have been used in conjunction with photometry from the Optical Gravitational Lens Experiment (OGLE-II) data base of SMC eclipsing binaries. Previously we reported results for 10 systems; in this second and concluding paper we present spectral types, masses, radii, temperatures, surface gravities and luminosities for the components of a further 40 binaries. The uncertainties are typically ± 10 per cent on masses, ± 4 per cent on radii and ± 0.07 on log L. The full sample of 50 OB-type eclipsing systems is the largest single set of fundamental parameters determined for high-mass binaries in any galaxy. We find that 21 of the systems studied are in detached configurations, 28 are in semidetached post-mass-transfer states, and one is a contact binary.

The overall properties of the detached systems are consistent with theoretical models for the evolution of single stars with SMC metal abundances ($Z \simeq 0.004$); in particular, observed and evolutionary masses are in excellent agreement. Although there are no *directly* applicable published models, the overall properties of the semidetached systems are consistent with them being in the slow phase of mass transfer in case A. About 40 per cent of these semidetached systems show photometric evidence of orbital-phase-dependent absorption by a gas stream falling from the inner Lagrangian point on the secondary star towards the primary star. This sample demonstrates that case-A mass transfer is a common occurrence amongst high-mass binaries with initial orbital periods $P \lesssim 5$ d, and that this slow phase has a comparable duration to the detached phase preceding it.

Each system provides a primary distance indicator. We find a mean distance modulus to the SMC of $18.91 \pm 0.03 \pm 0.1$ (internal and external uncertainties; $D = 60.6 \pm 1.0 \pm 2.8$ kpc). This value represents one of the most precise available determinations of the distance to the SMC.

Key words: binaries: close – binaries: eclipsing – binaries: general – binaries: spectroscopic – Magellanic Clouds.

1 INTRODUCTION

In a previous paper, Harries, Hilditch & Howarth (2003, hereafter HHH03) reported the first results of an observational programme to determine the fundamental parameters of stars in eclipsing binaries in the Small Magellanic Cloud (SMC). The rationale for this programme was fully described in HHH03, so it suffices to state here that the twin aims of this investigation are: to provide tests

of evolutionary models for high-mass binary stars, including those that undergo mass-exchanging interactions at early stages in their evolution; and to provide a set of primary distance indicators to determine the distance to, and line-of-sight depth of, the SMC, independently of all other distance calibrators. Since publication of HHH03, a Joint Discussion on 'Extragalactic Binaries' was held at the 2003 IAU General Assembly, and the papers presented there by many authors provide a broad overview of recent progress in this field (cf. Ribas & Giménez 2004).

HHH03 reported combined spectroscopic and photometric analyses of 10 relatively bright binaries; we now present follow-up

---

*E-mail: rwh@st-andrews.ac.uk

© 2005 RAS

observations and analyses of 40 additional targets. With such a large sample, we are insensitive to anomalous individual results (whether they arise from astrophysical effects or from problems with data, such as unresolved blending in the photometry), as well as gaining from simple statistical leverage that gives our results (and particularly our distance determination) very high weight. Furthermore, by introducing radial-velocity data, albeit of modest quality, we gain enormously over analyses based solely on light-curve solutions.

We summarize our observing programme in Section 2, and the spectroscopic and light-curve analyses in Section 3. Section 4 describes comparisons between the derived fundamental astrophysical parameters and evolutionary models for single stars and interacting binary stars, while Section 5 reviews distance determinations.

2 SPECTROSCOPIC OBSERVATIONS

Our programme was devised in 2000, aiming to exploit both the publication of the Optical Gravitational Lens Experiment photometric survey (OGLE-II; Udalski et al. 1998) and the commissioning of the two-degree-field (2dF) multi-object spectrograph on the 3.9-m Anglo-Australian Telescope (AAT). Extensive simulations for realistic expectations of time allocations showed that satisfactory orbital solutions should be obtainable for systems with $B \lesssim 16$ mag and orbital periods $P \lesssim 5$ d – constraints ensuring both adequate phase coverage for a reasonable sample, and sufficient signal-to-noise ratio (S/N) on the faintest targets (target S/N $\gtrsim 25$ per wavelength sample per observation). With these boundary conditions (and some further limitations introduced by practical constraints on the positioning of the 2dF optical fibres), we identified an initial sample of 169 SMC eclipsing binaries.

Our spectroscopy of these targets was obtained in two overlapping $2°$ diameter fields in the central regions of the SMC; details of the field centres, and checks on the astrometry, are described in HHH03. The data were taken using 2dF, in service mode (as is standard for this instrument). Each full observation consisted of two 1800-s integrations (on, typically, 100 targets simultaneously), plus arc and flat-field frames. Integration times of 1800 s were used for the target exposures, in seeing of typically 1.5–2 arcsec (cf. fibre diameters of 2 arcsec). We used the marginally better performing of the two spectrographs, with a 1200B grating providing a mean reciprocal dispersion of 1.1 Å pixel^{-1} and a resolution of 2 Å (the best available with this instrument). The wavelength range of the data is 3855–4910 Å, which ensures excellent coverage of the H, He I and He II lines that dominate the blue spectra of O and early B stars. The 2DFDR package (Lewis et al. 2002) was used with default settings to reduce all the data. The resultant spectra have S/N values ranging from ~20 to ~50.

From allocations of 12 nights over the 2001–2003 SMC observing seasons, worthwhile observations were secured on only five and a half nights. In consequence, the orbital phase coverage is generally poorer than planned, and for any given target depends on the orbital ephemeris and location (in our field overlap region or otherwise). The final data base has a total of more than 5200 spectra of 169 systems, with from five to 55 observations per target. Of these 169 systems, ~40 per cent do not have observations at or near quadrature phases (even in some cases with 55 spectra!). The remaining ~100 stars were studied in greater detail, using the procedures described in Section 3.

3 DATA ANALYSIS

The spectra were normalized by using an interactively defined spline fit to line-free continuum regions. (In examining each spectrum,

any remaining noise spikes caused by cosmic rays etc. were removed.) The spectra were then velocity-corrected to the heliocentric reference frame, and 'windowed' to isolate specific regions that include strong absorption lines, such as 4300–4500 Å (Hγ, He I $\lambda\lambda$4388, 4471). Orbital phases were calculated from photometric ephemerides[1] published by Wyrzykowski et al. (2004, based on four seasons of OGLE-II photometry) where available; otherwise we adopted results from Udalski et al. (1998, one and a half seasons).

3.1 Orbital parameters and component spectra

HHH03 described in detail the implementation of spectral disentangling codes, which permit precise and direct determinations of the orbital parameters of the binary components, without the need for intermediate steps (i.e. measurement of velocities for each component for every observation). We demonstrated that our codes, which implement the algorithm described by Simon & Sturm (1994), give results that agree well with orbital solutions based on the cross-correlation methods previously more frequently used for measuring radial velocities. Compared to these 'traditional' methods, spectral disentangling not only yields orbital solutions of better precision (or, indeed, orbital solutions from data that would not be amenable to cross-correlation analyses), but also gives disentangled average spectra for each binary component (at the expense of not returning 'per observation' velocity measurements). Some excellent review papers on the successes of spectral disentangling procedures are given by Hadrava (2004), Holmgren (2004) and Ilijic (2004).

3.1.1 Velocities

For each system, we searched for the best (least-squares) orbital solution by conducting grid searches in orbital semi-amplitudes (K_1, K_2), given the period and reference epoch. Circular orbits were assumed unless the light curve demonstrated eccentricity.[2] It was found that using data in the phase ranges 0.20–0.30 and 0.70–0.80 gave the most reliable and consistent results; as necessary, wider phase ranges were employed (0.15–0.35 and 0.65–0.85), but observations closer to conjunctions offer no useful leverage on orbital-velocity amplitudes.

At our spectral resolution, many binaries are clearly double-lined at quadrature phases, and well-defined orbital solutions are then readily obtained. However, the disentangling procedure is somewhat sensitive to the combination of orbital phase coverage and S/N in the data – important limiting factors in our sample. Where the grid search yielded multiple χ^2 minima, the consequent ambiguity could sometimes be safely resolved by further investigation (identifying preferred solutions on physical grounds). In all cases, sequentially finer grid searches were used to refine the solution.

---

[1] In consequence, when we refer to the 'primary component', we mean the star that is at superior conjunction at photometric phase zero (i.e. eclipsed at primary eclipse), which is the component with greater surface brightness – not necessarily the more massive component.

[2] In most cases, the light curves show no evidence of departures from circular orbits, with secondary eclipses at phase 0.50, and both eclipses of equal durations. In a few cases (discussed in Section 3.3), the orbits are, however, detectably eccentric, with secondary eclipses displaced from phase 0.50 by up to 0.10.

Table 1. Circular-orbit solutions (including 'non-Keplerian' corrections). Identifiers are from Udalski et al. (1998, PSF) and Wyrzykowski et al. (2004, DIA), and for each target there are n useful spectra, characterized by the stated S/N.

OGLE-PSF identifier	OGLE-DIA identifier	n	S/N	K_1 (km s^{-1})	K_2 (km s^{-1})	γ (km s^{-1})
1 099121	003851.98−733433.2	11	25	152 ± 11	259 ± 6	182 ± 15
4 056804	004633.14−732217.0	4	25	307 ± 5	280 ± 2	155 ± 5
4 103706	004725.50−732716.7	7	40	203 ± 6	359 ± 4	205 ± 13
4 110409	004700.19−731843.1	8	25	160 ± 11	247 ± 3	204 ± 18
4 163552	004753.24−731556.5	5	30	257 ± 11	275 ± 9	170 ± 3
5 026631	004859.84−731328.8	10	25	234 ± 8	239 ± 5	167 ± 6
5 060548	004835.40−725256.5	22	40	151 ± 4	187 ± 3	179 ± 5
5 095194	004950.42−731931.6	12	40	247 ± 23	215 ± 22	193 ± 6
5 140701	004943.08−725109.0	12	30	137 ± 9	179 ± 7	181 ± 9
5 180064	005044.74−731739.9	15	25	146 ± 3	222 ± 3	153 ± 6
5 208049	005045.00−725844.4	7	25	108 ± 3	226 ± 1	170 ± 4
5 243188	005118.78−733015.8	18	40	247 ± 14	362 ± 5	206 ± 5
5 255984	005129.62−732137.7	7	25	176 ± 38	292 ± 8	209 ± 3
5 277080	005111.68−730520.3	13	25	200 ± 10	308 ± 5	199 ± 23
5 300549	005123.57−725224.1	9	40	253 ± 9	369 ± 4	196 ± 5
5 305884	005120.17−724942.9	17	50	232 ± 14	252 ± 5	184 ± 4
6 011141	005203.96−731849.3	13	25	263 ± 4	281 ± 2	222 ± 11
6 152981	005241.88−724622.4	6	30	180 ± 4	276 ± 3	212 ± 9
6 180084	005342.42−732319.9	8	30	261 ± 22	305 ± 4	191 ± 4
6 251047	005344.05−723124.0	15	25	150 ± 3	221 ± 2	193 ± 5
6 311225	005402.00−724221.6	20	25	176 ± 3	312 ± 2	200 ± 4
6 319960	005405.26−723426.0	15	40	130 ± 11	204 ± 4	165 ± 20
7 066175	005438.22−723206.2	20	45	155 ± 14	264 ± 7	212 ± 3
7 120044	005531.57−724307.8	12	25	257 ± 6	258 ± 4	192 ± 6
7 142073	005554.44−722808.5	6	30	127 ± 10	254 ± 9	193 ± 7
7 189660	005637.30−724143.3	10	20	207 ± 10	310 ± 10	197 ± 2
7 193779	005621.80−723701.7	21	20	147 ± 13	289 ± 8	207 ± 3
8 087175	005830.98−723913.8	7	20	268 ± 21	300 ± 6	233 ± 10
8 104222	005825.08−721909.8	11	25	257 ± 14	277 ± 6	250 ± 2
8 209964	010016.05−721243.9	14	50	180 ± 6	234 ± 4	212 ± 18
9 010098	010052.90−724748.6	7	30	260 ± 23	339 ± 11	216 ± 8
9 047454	010052.04−720705.5	6	25	199 ± 21	271 ± 20	187 ± 12
9 064498	010117.26−724232.1	10	20	76 ± 9	235 ± 5	206 ± 7
10 094559	⋯	8	30	221 ± 16	267 ± 7	135 ± 7
10 108086	⋯	6	40	317 ± 20	375 ± 7	226 ± 15
10 110440	⋯	12	25	160 ± 36	292 ± 13	275 ± 12

Table 2. Eccentric-orbit solutions; ω is the longitude of periastron measured from the ascending node for the primary component. Semi-amplitudes include 'non-Keplerian' corrections. Identifiers are from Udalski et al. (1998, PSF) and Wyrzykowski et al. (2004, DIA).

OGLE-PSF identifier	OGLE-DIA identifier	n	S/N	K_1 (km s^{-1})	K_2 (km s^{-1})	γ (km s^{-1})	e	ω (deg)
5 311566	005134.85−724545.9	15	20	180 ±7	227 ±3	179 ±2	0.063 ±0.002	3.0 ±20.0
6 221543	005340.40−725222.0	22	25	200 ±1	205 ±21	186 ±11	0.113 ±0.004	316.0 ±1.9
7 255621	⋯	11	20	147 ±6	190 ±7	181 ±11	0.190 ±0.006	218.2 ±2.9
10 037156	⋯	14	30	231 ±3	265 ±2	239 ±10	0.013 ±0.009	202.0 ±27.0

The outcome of this survey was that, of the ∼100 systems examined in detail, 40 yielded reliable orbital parameters (in addition to the 10 systems already discussed in HHH03). The remainder did not provide sensible solutions, in that derived masses and distances were obviously discrepant (typically by factors of 2 or more). Spectroscopic solutions for the 40 'good' systems are given in Table 1 for circular orbits, and Table 2 for eccentric orbits. As the disentangling procedure returns only the semi-amplitudes, the tabulated systemic

velocities were determined separately, from a cross-correlation analysis of the disentangled mean spectra against a template spectrum of the O9V star 10 Lac, using the VCROSS code (Hill 1982). The values reported for each binary are the flux-weighted means of the two components. For eccentric orbits, values of eccentricity, e, and longitude of periastron, ω, were determined from the light-curve solutions (from the position of secondary eclipse and the durations of the two eclipses), and then held fixed in the spectroscopic solutions (because of selective phase coverage of the spectroscopy).[3]

The published velocity semi-amplitudes of the 10 systems studied by HHH03 were derived from spectra obtained only in the first, 2001, observing session. Since the numbers of usable spectra of these 10 systems has subsequently increased (and the original data have been re-reduced), new orbital solutions were conducted. The mean difference between the published and new semi-amplitudes is -2 ± 4 km s^{-1} (s.e.), and in no case did the original and new semi-amplitudes differ by more than the joint 1σ uncertainties. The mean difference in systemic velocities is -11 ± 4 km s^{-1} (s.e., HHH03 minus this paper). This difference reflects the fact that, in HHH03, the heliocentric velocity corrections (~ 6 km s^{-1}) were inadvertently applied with the incorrect sign, such that the previously published γ velocities should be corrected by $+12$ km s^{-1}. It is pleasing that this known mistake should be recovered in the data analysis, and that the expected uncertainties in the velocities ($\sim \pm 15$ km s^{-1}) should be consistent with the dispersion in the results. Other than the correction to the γ velocities, there is clearly no need to replace the HHH03 orbital solutions.

3.1.2 Spectral types

The separated component spectra that result from the disentangling procedure have S/N values that are $\sim \sqrt{n/2}$ greater than for each of the n individual observed spectra used in the analysis. We constructed disentangled spectra for each system by using all observations with orbital phases 0.15–0.35 and 0.65–0.85, and the full observed wavelength range.

These disentangled component spectra, shown in Figs 1 and 2, were classified by reference to the digital spectral atlas of Galactic O,B stars by Walborn & Fitzpatrick (1990) and to Lennon's (1997) SMC B-supergiant study. This task was performed independently by all three authors in order to assess the uncertainties associated with the spectral types. Typically we found that our classifications agreed to within one temperature subtype, and the adopted modal values for the primary components are given in Table 3. For the (normally weaker) spectra of the secondary components, we provide the range of spectral types assigned by the three authors. We found that the O–B1 stars were quite easy to classify, but that spectral classifications were more difficult for later B types as a result of the absence of He II lines and, in these low-metallicity stars, the lack of detectable Si II and other metal lines (see the discussion by Evans et al. 2004). However, our classifications of primary components all agree to within one subtype, and it is these classifications that establish the mean effective temperatures of the primary components (and hence the system absolute magnitudes; Section 5). In this sense the spectral types assigned to the secondary components are much

less important, although they do serve as consistency checks for the effective temperatures of the secondary components.

3.2 Light-curve analyses

The light-curve synthesis code LIGHT2 (Hill 1979; Hill & Rucinski 1993) was used for all analyses of the OGLE-II light curves.

3.2.1 Data sources

Our initial modelling made use of *I*-band photometry published by Udalski et al. (1998), based on one and a half seasons of OGLE observations reduced using standard techniques [point spread function (PSF) fits to stellar images]. This 'OGLE-PSF' data base afforded typically ~ 140 observations per light curve, with an average photometric error of 0.014 mag quoted by Udalski et al. (1998). The overall rms scatter of the observations about the model fits was 0.019 mag, ranging from 0.011 to 0.028 mag for individual systems, but some of the OGLE-PSF light curves were not particularly well sampled, with some eclipses defined by as few as 10 observations.
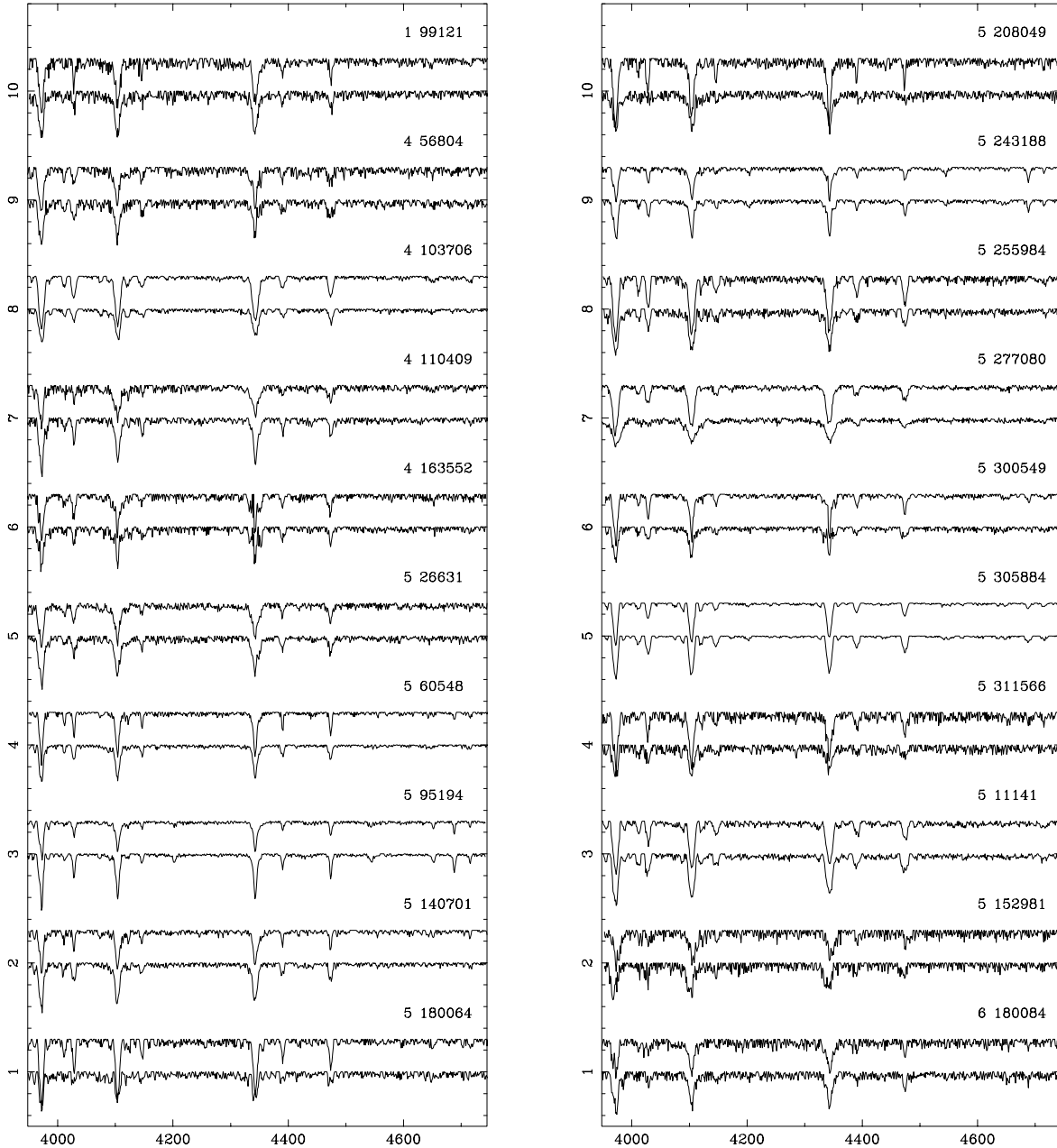
Wyrzykowski et al. (2004) subsequently published results from four seasons of OGLE *I*-band photometry, reduced by using the 'difference image analysis' (DIA) technique described by Zebrun et al. (2001). Not all our sample stars are included in this OGLE-DIA data base, but for those that are there is improved accuracy in the ephemerides (though most changes are quite small, ~ 1–2 parts in 10^5 for P_{orb}); the light curves are better sampled (typically ~ 300 observations per target); and the re-reduced photometry is more accurate (quoted average photometric error 0.011 mag), at least for uncrowded sources.

We therefore repeated the entire analysis for the 35 systems in our sample that have DIA photometry, all of which are reported to be 'uncrowded' sources (Wyrzykowski et al. 2004). In general, we found only small changes in the system parameters, but improved accuracy; the overall rms scatter of the DIA observations about the model fits is 0.014 mag, ranging from 0.005 to 0.025 mag for individual systems. (One exception, 5 311566, is discussed in Section 3.3.17). The five systems for which we have only the PSF photometry still have quite well-defined light curves, and satisfactory solutions.

3.2.2 Methodology

To carry out the light-curve solutions, mass ratios were fixed from the spectroscopic solutions, and standard values were used for limb-darkening coefficients (appropriate to the local temperatures at each grid point over the surfaces of both stars in each binary), for gravity-darkening exponents (for stars with radiative envelopes), and for albedos and electron scattering fractions (from Hill & Hutchings 1971). Synchronous rotation was assumed in all cases.

We solved each light curve for the two stellar radii, the orbital inclination and the temperature of the secondary component (strictly the *I*-band flux ratio between the two stars, but characterized by blackbody fluxes at the appropriate temperatures and effective wavelengths). The temperature of the primary component was fixed at the value corresponding to its assigned spectral type, and the default starting assumption for each solution was that each system is composed of stars that are detached from their respective Roche lobes. Semidetached configurations, with the secondary star filling its Roche lobe, were adopted only when the detached solutions indicated a secondary star volume of 98–100 per cent of its Roche lobe.

---

[3] The light-curve solutions require input (the mass ratio) from the spectroscopic orbit, and the spectroscopic solutions require input ('non-Keplerian' corrections, as well as e and ω) from the light-curve solutions. The velocity corrections rarely exceed 5 km s^{-1} and a single iteration between light-curve and spectroscopic solutions gave convergence (including any adjustments to e and ω).
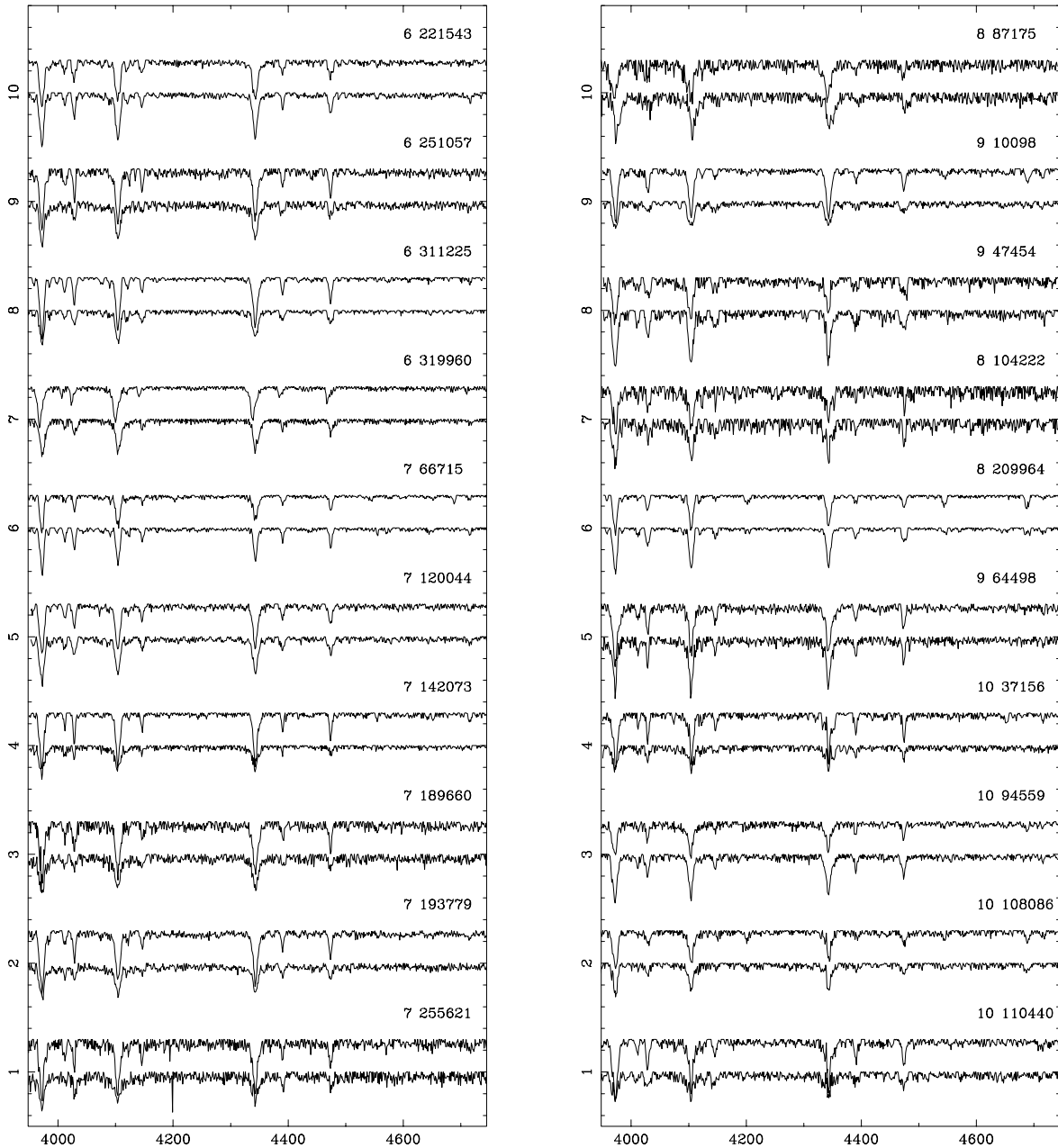
Figure 1. Disentangled component spectra for 20 binaries; results for the remainder of the sample are shown in Fig. 2. The normalized spectra are plotted as relative flux, with the secondary offset by −0.5 continuum units for clarity. Wavelengths are in Å; the strong absorption lines include Hε, Hδ, Hγ and He I λλ4026, 4144, 4388, 4471, 4713, as well as He II λλ4200, 4542, 4686 in some cases.

The disentangled spectra offer an independent constraint on the flux ratio: requiring the overall relative strengths of the components' line spectra to match expectations based on spectral type gives an estimate of the continuum flux ratio (in the *B* band). Because this is a relatively blunt tool, and because the binaries studied in this paper are fainter than those discussed in HHH03 (and consequently their spectra have lower S/N values), we did not impose these spectroscopic flux ratios on the light-curve solutions, but used them, where necessary, to distinguish between competing, and sometimes statistically indistinguishable, solutions to the *I*-band light curves with detached or semidetached configurations.[4]

Table 3 gives the adopted values for optimized parameters, and the observed and model light curves are shown in Figs 3–6, together with the corresponding (O−C) plots. In 90 per cent of cases, the (O−C) curves show no systematic phase-dependent deviations, demonstrating that satisfactory fits have been obtained; the few exceptions are discussed individually below. We provide reduced chi-squared values, χ_ν^2, in Table 3, as a quantitative measure of the quality of each fit to each set of data.

---

[4] For a given system, detached solutions almost invariably imply flux ratios

that are larger than those of semidetached solutions, since the differences in radii of the two stars are generally larger.

Figure 2. Disentangled component spectra for 20 binaries; results for the remainder of the sample are shown in Fig. 1. The normalized spectra are plotted as relative flux, with the secondary offset by −0.5 continuum units for clarity. Wavelengths are in Å; the strong absorption lines include Hε, Hδ, Hγ and He I λλ4026, 4144, 4388, 4471, 4713, as well as He II λλ4200, 4542, 4686 in some cases.

3.3 Notes on individual binaries

In this section we comment on various aspects of individual solutions. Targets are identified by entries in the Udalski et al. (1998) catalogue and, in parentheses, the OGLE DIA catalogue (Zebrun et al. 2001).

Of the systems considered here, several have had light-curve solutions attempted by Clausen et al. (2003; 5 140701), by Wyithe & Wilson (2001, 2002; 4 103706, 4 163552, 7 66175, 7 255621, 8 87175), or by Graczyk (2003; 4 103706, 4 163552, 5 311566, 6 221543, 8 104222). Because their solutions were unconstrained by spectroscopy, we do not make detailed comparisons with, or comments on, their results, which must be regarded as substantially less secure than ours.

3.3.1 1 99121 (DIA 003851.98−733433.2)

From 11 spectra in the wider phase ranges 0.15–0.35 and 0.65–0.85, a single minimum was found in the disentangling solution. The light-curve solution converged immediately to a semidetached configuration, with a photometric flux ratio of 1.2 confirmed by the relative strengths of the spectral lines. The model fits the eclipse curves well, but the observational data just before first contact of primary eclipse are depressed relative to those just after fourth contact, and this asymmetry is reflected in the value of χ^2_ν. Such depressions in light curves occurring just before the onset of primary eclipse are observed quite frequently in semidetached (Algol-type) binaries and are indicative of absorption by the gas stream from the inner Lagrangian point of the Roche lobe filling secondary star falling

Table 3. Light-curve solutions. System types (column 2) are detached, semidetached, or (in one case) in contact. Primary temperatures are based on spectral types; secondary temperatures characterize the *I*-band flux ratio (Section 3.2). Radii are given in units of the semimajor axis of the relative orbit; for semidetached systems the radii of the secondary components are fixed by the mass ratio.

| OGLE-PSF identifier | System type | Spectral type | | T_{eff} (K) | | Mean radius | | Inclination (deg) | Mass ratio | χ_ν^2 |
		primary	secondary	primary	secondary	primary	secondary			
1 099121	sd	B0.5	B1–3	27800	15820 ± 165	0.248 ± 0.006	0.332	85.4 ± 0.3	1.704	2.54
4 056804	d	B0	B0–2	30100	24200 ± 350	0.307 ± 0.006	0.368 ± 0.005	70.5 ± 0.2	0.912	0.73
4 103706	d	B0.5	B0–1	27800	27050 ± 430	0.345 ± 0.007	0.261 ± 0.007	75.8 ± 0.4	1.768	1.29
4 110409	sd	B1	B0.5–3	25500	15390 ± 160	0.177 ± 0.007	0.341	76.8 ± 0.3	1.544	2.80
4 163552	d	B1	B0–3	25500	25390 ± 190	0.320 ± 0.003	0.312 ± 0.004	78.3 ± 0.1	1.070	0.82
5 026631	sd	B1	B1–3	25500	17130 ± 300	0.341 ± 0.002	0.377	61.5 ± 0.1	1.021	0.92
5 060548	sd	B0	B0.5–2	30100	17480 ± 250	0.314 ± 0.002	0.360	65.2 ± 0.1	1.238	1.92
5 095194	d	O9	O9	33800	32600 ± 100	0.252 ± 0.002	0.298 ± 0.002	65.3 ± 0.1	0.870	0.39
5 140701	d	B1.5	B2	23500	15310 ± 230	0.345 ± 0.005	0.307 ± 0.008	81.7 ± 0.6	1.307	1.52
5 180064	d	B1	B1	25500	17110 ± 1210	0.275 ± 0.013	0.222 ± 0.014	64.6 ± 0.2	1.521	0.53
5 208049	sd	B1	B1–5	25500	14270 ± 160	0.306 ± 0.002	0.315	67.6 ± 0.1	2.093	0.86
5 243188	sd	O8.5	O9–B0	35300	32110 ± 50	0.319 ± 0.003	0.345	79.9 ± 0.1	1.466	1.01
5 255984	d	B1	B1–2	25500	25050 ± 950	0.314 ± 0.019	0.255 ± 0.015	64.8 ± 0.2	1.659	0.81
5 277080	sd	B1	B2	25500	15890 ± 150	0.253 ± 0.004	0.341	76.8 ± 0.2	1.540	1.55
5 300549	sd	B0	B0–2	30100	16050 ± 260	0.357 ± 0.003	0.346	66.9 ± 0.1	1.458	0.78
5 305884	d	O9	O9	33800	32500 ± 240	0.340 ± 0.005	0.286 ± 0.013	65.8 ± 0.6	1.086	1.63
5 311566	d	B0	B0–3	30100	28730 ± 650	0.165 ± 0.004	0.121 ± 0.007	86.4 ± 0.9	1.261	5.57
6 011141	d	B0	B0–1	30100	22740 ± 460	0.350 ± 0.002	0.348 ± 0.003	61.3 ± 0.2	1.068	0.64
6 152981	d	B1	B1–3	25500	20160 ± 150	0.270 ± 0.003	0.341	79.9 ± 0.1	1.533	1.75
6 180084	d	B0.5	B0–2	27800	27930 ± 350	0.346 ± 0.005	0.337 ± 0.006	77.0 ± 0.1	1.169	0.79
6 221543	d	B1	B1–2	25500	26600 ± 230	0.193 ± 0.014	0.166 ± 0.016	84.1 ± 0.4	1.025	0.91
6 251047	sd	B1.5	B3	23500	13520 ± 90	0.249 ± 0.005	0.345	82.5 ± 0.2	1.473	1.01
6 311225	sd	B0	B0.5–2	30100	23500 ± 280	0.323 ± 0.001	0.329	61.2 ± 0.1	1.773	0.89
6 319960	sd	B1	B1–2	25500	16300 ± 150	0.162 ± 0.003	0.339	75.5 ± 0.2	1.569	1.57
7 066175	sd	O9.5	B0.5–1	32200	25350 ± 410	0.253 ± 0.003	0.333	74.1 ± 0.1	1.703	4.79
7 120044	d	B1	B1	25500	25560 ± 410	0.325 ± 0.005	0.318 ± 0.007	65.1 ± 0.1	1.004	0.81
7 142073	sd	B0	B0.5–1.5	30100	21010 ± 280	0.394 ± 0.003	0.319	81.2 ± 0.1	2.000	2.52
7 189660	sd	B1	B1–2	25500	16910 ± 160	0.307 ± 0.004	0.343	78.1 ± 0.1	1.498	1.52
7 193779	sd	B1	B1–2	25500	17160 ± 220	0.377 ± 0.003	0.321	69.5 ± 0.1	1.966	0.94
7 255621	d	B1	B1–3	25500	23370 ± 890	0.177 ± 0.009	0.125 ± 0.020	85.4 ± 1.5	1.293	1.64
8 087175	d	B1	B1–2	25500	24740 ± 510	0.353 ± 0.010	0.345 ± 0.011	77.0 ± 0.2	1.119	1.43
8 104222	d	B1	B1–2	25500	25260 ± 790	0.315 ± 0.021	0.312 ± 0.021	84.1 ± 0.3	1.078	2.03
8 209964	sd	O8	O9	36300	26460 ± 270	0.255 ± 0.005	0.355	64.4 ± 0.4	1.300	1.38
9 010098	sd	O9	B0	33800	31840 ± 90	0.357 ± 0.001	0.355	67.5 ± 0.1	1.304	0.74
9 047454	sd	B1	B1–2	27800	16890 ± 300	0.264 ± 0.003	0.352	66.9 ± 0.2	1.362	1.94
9 064498	sd	B1	B0.5–2	25500	17060 ± 360	0.301 ± 0.009	0.285	64.6 ± 0.4	3.092	0.80
10 037156	d	O9.5	B0.5–2	32200	31300 ± 370	0.266 ± 0.005	0.163 ± 0.017	78.0 ± 1.0	1.147	1.06
10 094559	sd	B0	B1	30100	23890 ± 360	0.273 ± 0.007	0.362	80.6 ± 0.4	1.208	3.96
10 108086	c	O9	O9.5–B0	33800	29900 ± 1000	0.466 ± 0.002	0.438 ± 0.002	82.8 ± 0.1	1.183	1.88
10 110440	d	B1	B2	25500	21400 ± 470	0.274 ± 0.014	0.253 ± 0.010	74.5 ± 0.3	1.825	0.48

towards the primary star. Just before primary eclipse, the gas stream is seen in projection across the face of the primary component, and causes the extra absorption.

3.3.2 4 56804 (DIA 004633.14−732217.0)

Spectra in the wider phase ranges yielded multiple χ^2 minima in the disentangling solutions, none of which gave physically sensible results, but the four spectra closest to quadratures gave a mass ratio (primary/secondary) $q < 1.0$, and the resultant light-curve solution provides an excellent fit to the data ($\chi_\nu^2 = 0.73$) and a *B*-band flux ratio of unity, consistent with the spectra.

3.3.3 4 103706 (DIA 004725.50−732716.7)

A simple disentangling solution from spectra in the narrower phase ranges (0.20–0.30, 0.70–0.80) coupled with a detached solution to this well-defined light curve provides a flat (O−C) curve, rms scatter of 0.013 mag, and $\chi_\nu^2 = 1.29$. The light-curve solution predicts a *B*-band flux ratio of 1.8, consistent with the spectra.

3.3.4 4 110409 (DIA 004700.19−731843.1)

There were no spectroscopic observations very close to phases 0.25 or 0.75, but by using the complete spectra in the wider phase ranges a unique solution was found, at a mass ratio of 1.544. The light curve is asymmetric, with the first maximum being 0.03 mag brighter than
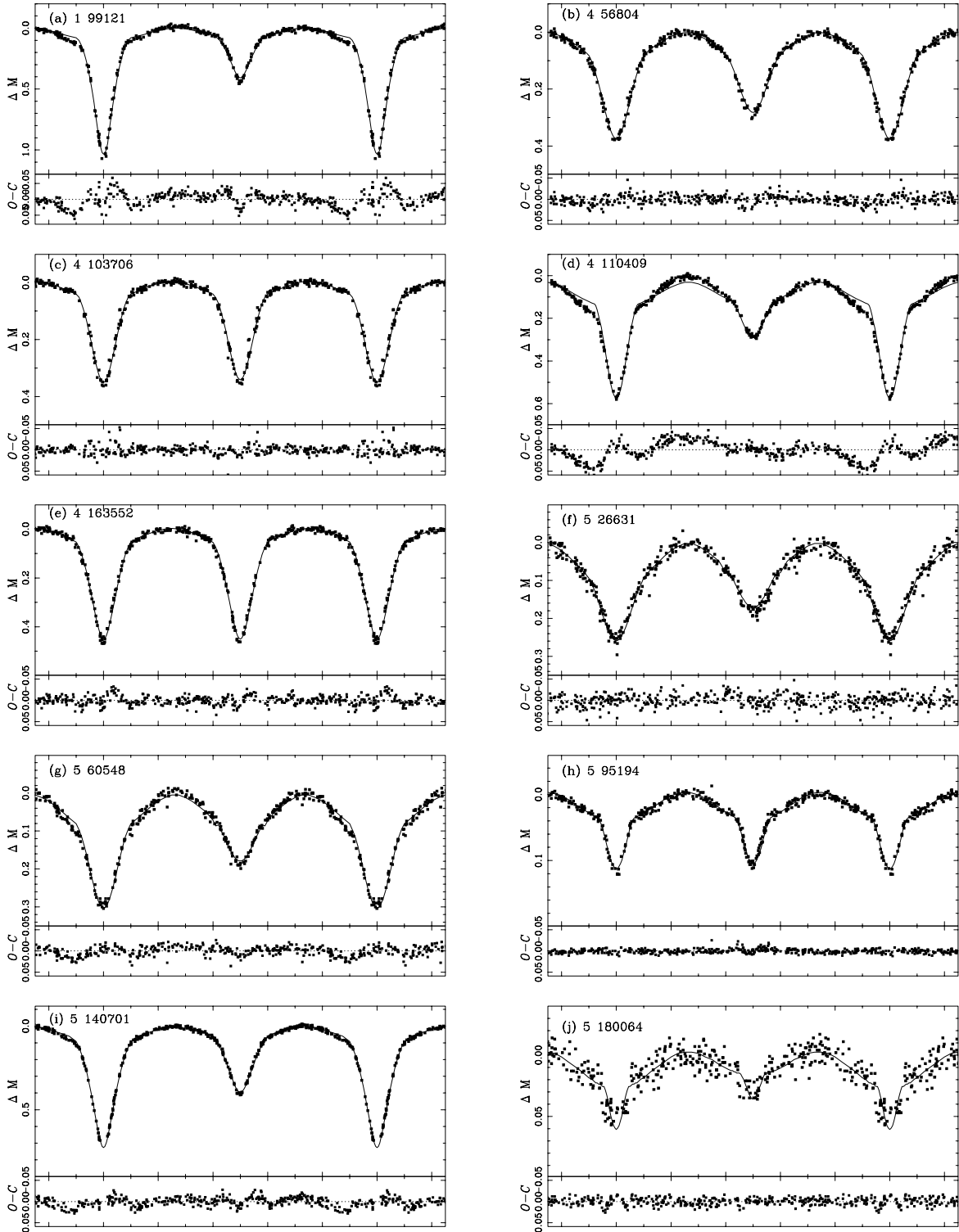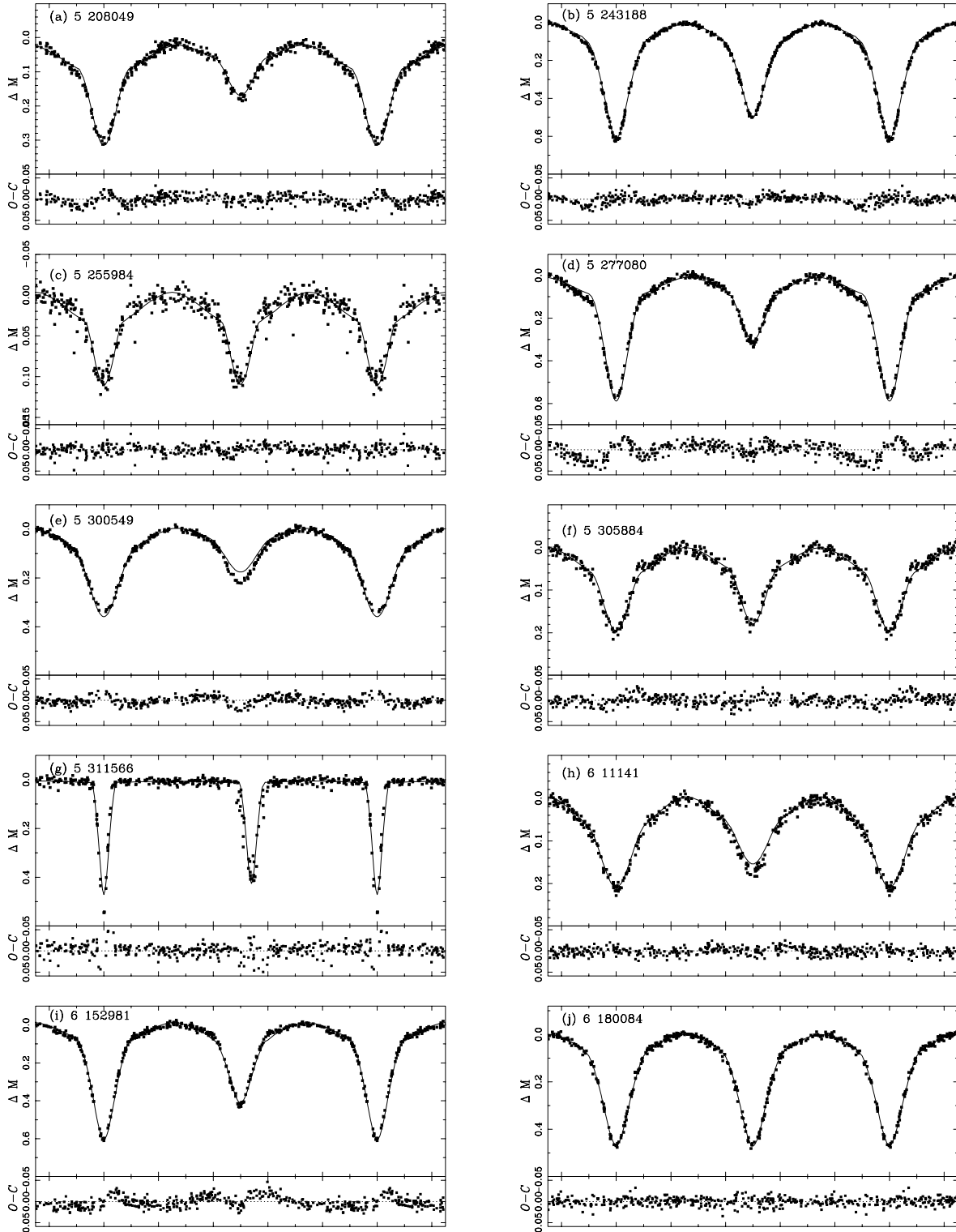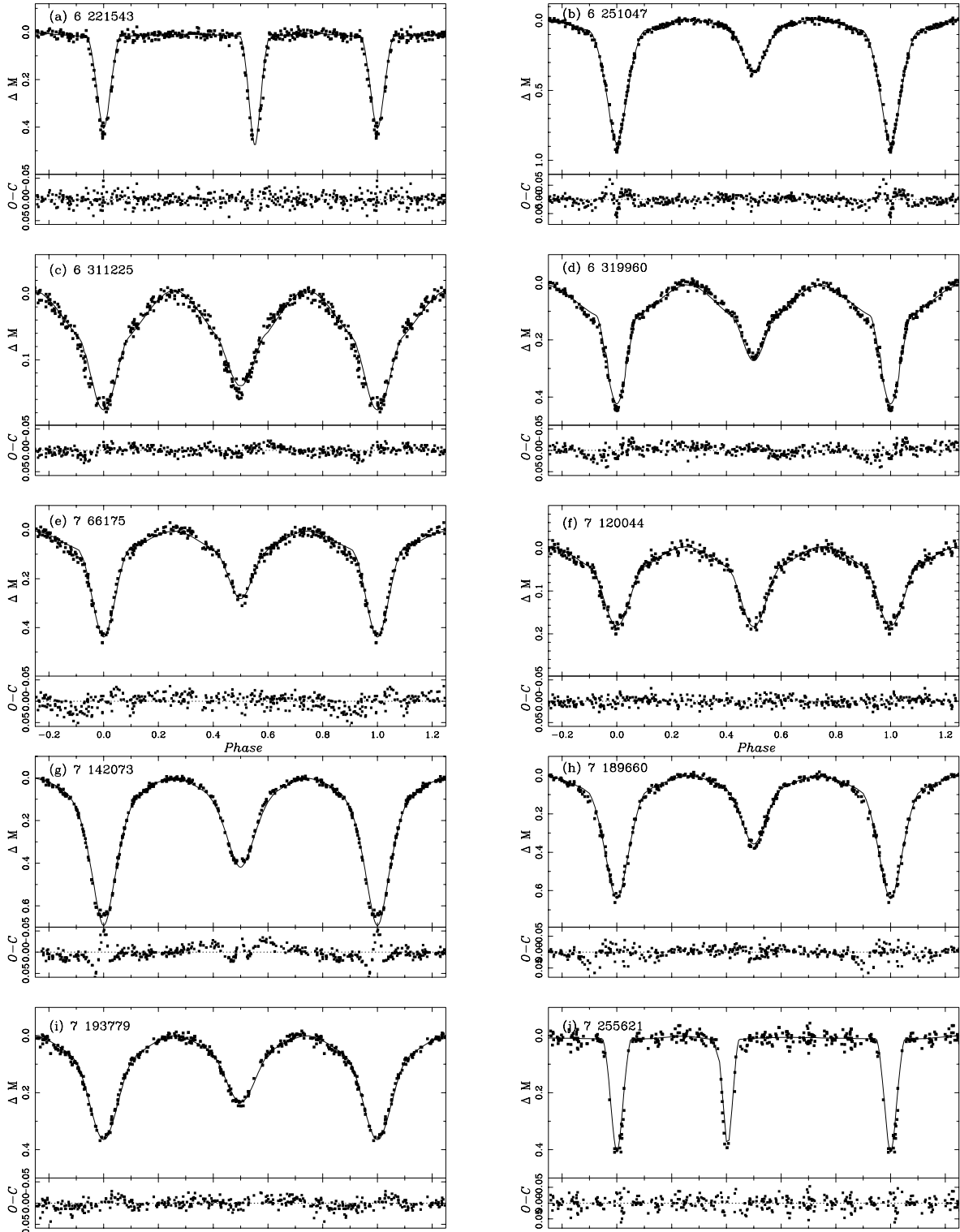
Figure 3. The *I*-band light curves from OGLE-II (data points), plotted over 1.5 cycles, and model fits from LIGHT 2 (solid lines) for 10 SMC binaries (further results are shown in the three accompanying figures). Note that the vertical scale varies between panels. The (O−C) scatter about the fit to each light curve is shown in the lower subpanel.

the second, which limits the quality of the light-curve fit, as reflected in the reduced chi-squared of 2.80. Nevertheless, the shapes of both eclipses are well modelled, providing sensible stellar radii for this semidetached system. The implied photometric flux ratio of 0.6 agrees very well with the spectroscopic value.

3.3.5 4 163552 (DIA 004753.24−731556.5)

This is an obviously double-lined system giving a simple disentangling solution and a good detached solution to the well-defined light curve, yielding an rms scatter of 0.011 mag and $\chi_\nu^2 = 0.82$. The photometric flux ratio of 1.0 agrees with the spectra.

Figure 4. The *I*-band light curves from OGLE-II (data points), plotted over 1.5 cycles, and model fits from LIGHT 2 (solid lines) for 10 SMC binaries (further results are shown in the three accompanying figures). Note that the vertical scale varies between panels. The (O−C) scatter about the fit to each light curve is shown in the lower subpanel.

3.3.6 5 26631 (DIA 004859.84−731328.8)

Disentangling solutions of the 10 spectra in the narrower phase ranges resulted in several χ^2 minima, but only one (with a mass ratio of unity) gave physically sensible results when combined with the light-curve analysis. Statistically indistinguishable solutions to the light curve were obtained with a detached configuration (the primary being the larger star), and with a semidetached configuration (with the secondary being larger). In the detached case, the primary fills 97 per cent of its Roche lobe, the expected *B*-band flux ratio is 2.7, and the resultant astrophysical parameters are inconsistent with evolution models for single stars. In the semidetached case,
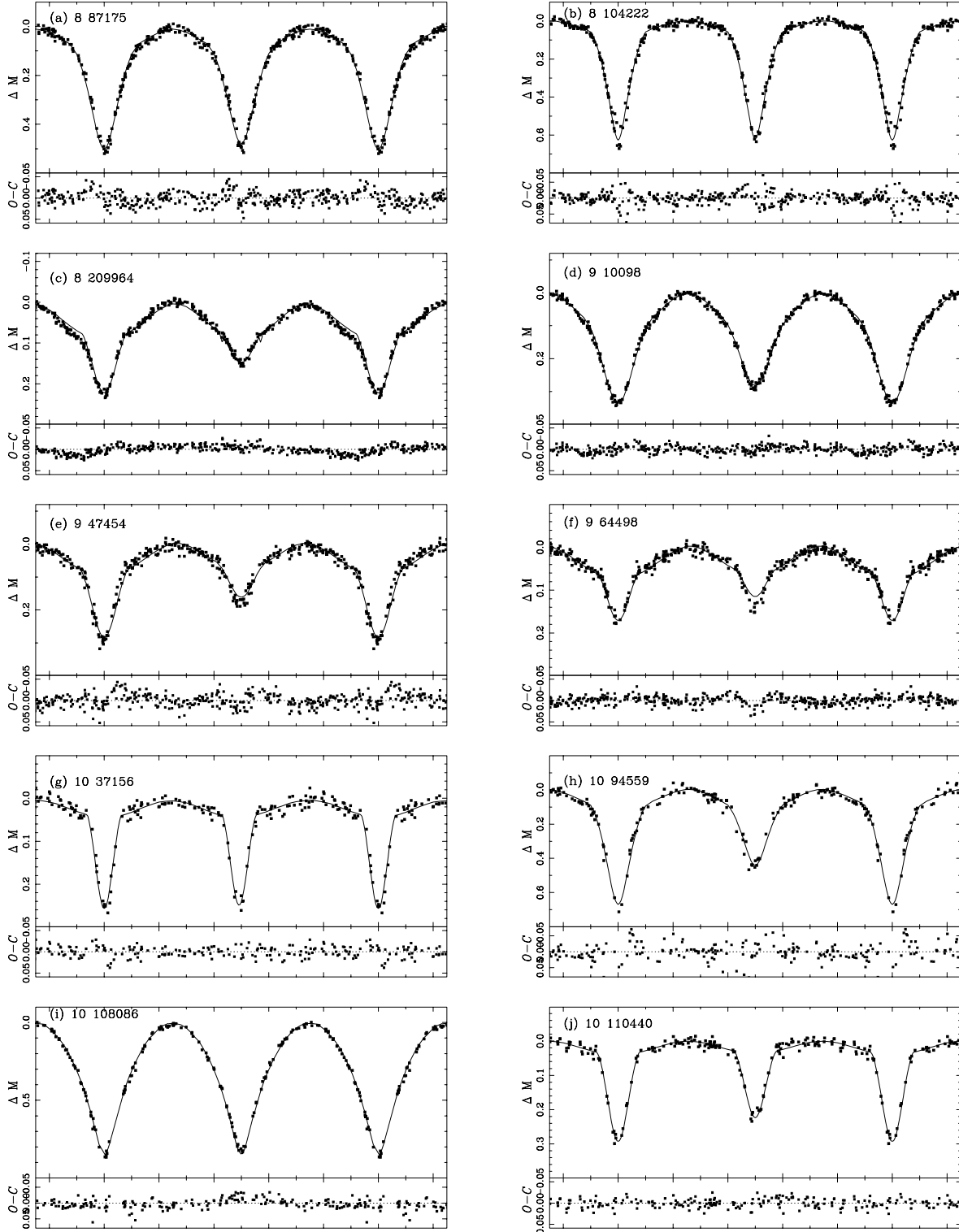
Figure 5. The *I*-band light curves from OGLE-II (data points), plotted over 1.5 cycles, and model fits from LIGHT 2 (solid lines) for 10 SMC binaries (further results are shown in the three accompanying figures). Note that the vertical scale varies between panels. The (O−C) scatter about the fit to each light curve is shown in the lower subpanel.

the secondary fills its Roche lobe and the *B*-band flux ratio of 1.4 is consistent with the spectra. The semidetached solution was therefore adopted, giving a light-curve fit showing an rms scatter of 0.016 mag and $\chi_\nu^2 = 0.92$.

3.3.7 5 60548 (DIA 004835.40−725256.5)

A simple disentangling solution was obtained from 22 spectra in the wider phase ranges. The light-curve solution converged to a semidetached configuration with a photometric flux ratio of 1.7, consistent

Figure 6. The *I*-band light curves from OGLE-II (data points), plotted over 1.5 cycles, and model fits from LIGHT 2 (solid lines) for 10 SMC binaries (further results are shown in the three accompanying figures). Note that the vertical scale varies between panels. The (O−C) scatter about the fit to each light curve is shown in the lower subpanel.

with the spectra. Although the rms scatter of the observations about the model fit is small, at 0.011 mag, the χ^2_ν value of 1.92 reflects the small asymmetry in the observed curve just before first contact of primary eclipse.

3.3.8 5 95194 (DIA 004950.42−731931.6)

The two O-type stars are clearly seen in double-lined spectra, with a spectroscopic flux ratio of 0.8. The disentangling solution was obtained from 12 spectra in the wider phase ranges, mostly covering

first quadrature, and demonstrate that the secondary component is the more massive star. The light-curve solution ($\chi^2_\nu = 0.39$) was then determined with a secondary component larger than the primary but a little cooler, as indicated by primary eclipse being ∼0.015 mag deeper than secondary eclipse. The resulting *B*-band flux ratio is consistent with that seen in the spectra.

3.3.9 5 140701 (DIA 004943.08−725109.0, HV 11284)

A simple disentangling solution from 12 spectra in the wider phase ranges led to a detached configuration from the light-curve solution, and a photometric flux ratio of 2.3, consistent with the spectra. The rms scatter of 0.011 and χ^2_ν of 1.52 indicate a good solution.

3.3.10 5 180064 (DIA 005044.74−731739.9)

The 15 spectra covering both quadratures in the narrower phase ranges provided a simple and well-defined disentangling solution, despite the substantial flux ratio (>2). The light curve has a low amplitude (0.08 mag), but the model fit is excellent, with an rms scatter of 0.009 mag, and χ^2_ν of 0.53. The predicted *B*-band flux ratio of 2.7 is consistent with the spectra.

3.3.11 5 208049 (DIA 005045.00−725844.4)

All but one of the 16 spectra used in the first disentangling solution lie in the phase range 0.65–0.85, and several minima were found. The quoted result is from the spectra in the phase range 0.70–0.80, which provided the best light-curve solution, yielding a semide-tached configuration with a photometric flux ratio of 1.4 (consistent with the spectra). The quality of the fit is reasonable, with rms scatter of 0.016 mag, and $\chi^2_\nu = 1.67$.

3.3.12 5 243188 (DIA 005118.78−733015.8)

The best disentangling solution was obtained with 18 spectra from the wider phase ranges of 0.15–0.35 and 0.65–0.85, and the large-amplitude light curve yielded alternative detached and semidetached solutions with different flux ratios. The semidetached solution re-quires a flux ratio of 0.85, which is consistent with the spectra (the secondary's spectral lines are slightly stronger than those of the pri-mary). The quality of the fit to the light curve is excellent, with an rms scatter of 0.009 mag and $\chi^2_\nu = 1.01$, and a small dip just before first contact of primary eclipse.

3.3.13 5 255984 (DIA 005129.62−732137.7)

Spectra in the phase ranges 0.20–0.30 and 0.70–0.80 yielded a single sensible disentangling solution, and the low-amplitude (0.12 mag) light curve provides a good detached solution with a flat (O−C) curve, rms scatter of 0.011 mag, and $\chi^2_\nu = 0.81$. The model flux ratio of 1.5 is consistent with the spectra.

3.3.14 5 277080 (DIA 005111.68−730520.3)

A simple disentangling solution from 13 spectra in the narrower phase ranges, and a semidetached configuration for the light-curve solution, provide the best match to the flux ratio of unity seen in the spectra. The (O−C) curve has some deviations around first contact of primary eclipse, reflected in the rms scatter of 0.016 mag and $\chi^2_\nu = 1.55$. None the less, the overall fit appears to be good.

3.3.15 5 300549 (DIA 005123.57−725224.1)

There are indications of emission lines at Hγ, and for the disen-tangling solution we used only the He I lines, with phase ranges 0.20–0.30 and 0.70–0.80. The light curve required a phaseshift of −0.0050 before a good semidetached configuration was obtained, with a photometric flux ratio of 1.2, matching the line spectra. The rms scatter is 0.010 mag, with $\chi^2_\nu = 0.78$.

3.3.16 5 305884 (DIA 005120.17−724942.9)

The 17 spectra in the narrower phase ranges give one physically sensible solution, and the light-curve analysis provides a reasonable fit with rms scatter of 0.011 mag and $\chi^2_\nu = 1.63$. The predicted *B*-band flux ratio of 1.5 is consistent with the spectra.

3.3.17 5 311566 (6 67289, DIA 005134.85−724545.9)

This system falls in the overlap of two OGLE fields, and so has two identifiers. In our initial analyses we solved the PSF light curves for '5 311566' and '6 67289' both separately and combined, obtaining closely similar results.

The DIA light curve is very similar in appearance to the PSF results, clearly showing an eccentric orbit with deep eclipses, but unfortunately the number of observations defining the shapes of both eclipses is very limited (Fig. 4g), and this factor constrains the quality of the overall solution. The light curve was solved as an obvious detached system at a mass ratio of unity for the usual set of parameters together with *e*, ω. An orbital solution with these *e*, ω values fixed provided the semi-amplitudes, and the light-curve solution was slightly revised. The paucity of observations through eclipses may contribute to the high rms of 0.036 mag and $\chi^2_\nu = 5.57$, by far the worst in the entire sample.

3.3.18 6 11141 (DIA 005203.96−731849.3)

A simple disentangling solution allowed a straightforward solution for the light curve, which has a rather low amplitude of 0.22 mag. The (O−C) curve is flat, with an rms scatter of 0.009 mag and $\chi^2_\nu = 0.64$. The photometric flux ratio of 1.7 is consistent with the spectra.

3.3.19 6 152981 (DIA 005241.88−724622.4)

Only the first-quadrature phases for this binary were observed, but an orbit solution was obtained straightforwardly. The light curve has deep eclipses, and a semidetached configuration was required to obtain the *B*-band flux ratio of 0.8 seen in the spectra. The rms scatter about the model fit is 0.014 mag, whilst $\chi^2_\nu = 1.75$ reflects apparent slight asymmetries in the eclipse curves. A slight phaseshift (∼0.002) may improve the fit.

3.3.20 6 180084 (DIA 005342.42−732319.9)

Only eight spectra in the wider phase ranges were available for this system, but these gave a unique solution, indicating stars of similar masses. The well-defined light curve with deep eclipses is accurately modelled, giving an rms scatter of 0.014 mag and $\chi^2_\nu = 0.79$, and the photometric flux ratio of unity is confirmed by the spectra.

3.3.21 6 221543 (DIA 005340.40−725222.0)

For the second system in the sample with an obviously eccentric orbit, the light curve was solved at an initial mass ratio of unity and including e, ω as free parameters. The spectroscopic solution was obtained with these e, ω values fixed, from 22 spectra. The derived mass ratio of 1.025 clearly did not significantly change the subsequent re-solution of the light curve, which yields an rms scatter of 0.015 mag and $\chi_\nu^2 = 0.91$. The photometric flux ratio of 1.3 is consistent with the spectra.

3.3.22 6 251047 (DIA 005344.05−723124.0)

A simple disentangling solution was secured, and the subsequent light-curve solution proved to be straightforward, with a semidetached configuration providing a photometric flux ratio of 1.1. The DIA light curve is free of the obvious contamination seen in the PSF results, although the derived parameters are similar. A phaseshift of 0.0020 was applied to the DIA light curve to improve the fit to the light curve, which shows some anomalies in primary eclipse but a good fit through secondary eclipse. The rms scatter is 0.022 mag, and $\chi_\nu^2 = 1.01$.

3.3.23 6 311225 (DIA 005402.00−724221.6)

A total of 20 spectra cover both quadratures well, but more than one solution was found. The adopted light-curve solution is for a semidetached configuration with a B-band flux ratio of 1.4, consistent with the spectra. The rms scatter of 0.009 mag and $\chi_\nu^2 = 0.89$ indicate a good solution to this shallow light curve, which nevertheless has a small asymmetry in the descending branch of primary eclipse.

3.3.24 6 319960 (DIA 005405.26−723426.0)

Only the second-quadrature phases were sampled, by 15 spectra, but a solution was obtained straightforwardly. The spectra indicate a flux ratio of 0.4 and a semidetached configuration. This result is confirmed in the light-curve solution, which yields a reasonable fit, with rms scatter of 0.012 mag and $\chi_\nu^2 = 1.57$. Again, there is a small dip just before first contact of primary eclipse.

3.3.25 7 66175 (DIA 005438.22−723206.2)

A total of 20 spectra in the wider phase ranges, but mostly from second quadrature, were used to establish the orbital solution of this obviously double-lined system with a flux ratio less than unity. The light-curve solution gives a good match to the overall shape of the curve, but there is a significant depression just before first contact of primary eclipse, which is reflected in $\chi_\nu^2 = 4.79$, although the rms scatter is tolerable at 0.016 mag. The light-curve solution for a semidetached configuration correctly predicts the spectroscopic flux ratio.

3.3.26 7 120044 (DIA 005531.57−724307.8)

An obvious double-lined system with well-sampled quadratures yielded a simple disentangling solution from 12 spectra. The light curve is also well modelled, by a model with a detached configuration, giving a flat (O−C) curve, rms scatter of 0.009 mag and $\chi_\nu^2 = 0.81$, and a flux ratio of unity, matching the spectroscopic value.

3.3.27 7 142073 (DIA 005554.44−722808.5)

Various competing χ^2 minima in the disentangling solution from 19 spectra in the wider phase ranges were reduced to one physically sensible solution with the use of the six spectra in the narrower phase ranges. The resulting mass ratio of 2.0 provides a solution to the well-defined light curve with deep eclipses as a semidetached configuration and a flux ratio of 2.7, consistent with the spectra. The model fit is generally good, with rms scatter of 0.016 mag, but a χ_ν^2 as large as 2.52 reflects the fact that the primary eclipse in the model is too deep by 0.05 mag.

3.3.28 7 189660 (DIA 005637.30−724143.3)

A set of 10 spectra in the wider phase ranges yielded a sensible orbit solution. A phaseshift of +0.0050 was required to improve the model fit to the light curve, which has deep eclipses. The overall rms scatter is 0.016 mag, and $\chi_\nu^2 = 1.52$ reflects the fact that there is, again, a small dip in the observed curve just before first contact of primary eclipse in this semidetached system. The photometric flux ratio of 1.3 is consistent with the spectra.

3.3.29 7 193779 (DIA 005621.80−723701.7)

Both quadrature phases were well sampled, with 21 spectra, and the orbit solution was simple. The light curve is well defined, and the model fit to the data is very good, yielding a flat (O−C) curve, an rms scatter of 0.012 mag and $\chi_\nu^2 = 0.94$, and a flux ratio of 2.3, which is consistent with the spectra.

3.3.30 7 255621 (8 30634)

A second target that occurs in two OGLE fields, and the third system in this sample with an obviously eccentric orbit, 7 255621 has a large orbital eccentricity ($e = 0.198$). As with the other eccentric-orbit systems in this sample, the number of observations defining the narrow eclipses is very limited, and this factor handicaps the accuracy of the solution. We solved the PSF light curves for 7 255621 and for 8 30634 separately, confirming agreement (particularly in the determinations of e, ω). We then combined the data into a single light curve with the 7 255621 ephemeris, since there were no obvious zero-point differences in the two data sets. The combined light curve was solved for e, ω, and the results adopted in the disentangling solution using 11 spectra in the wider phase ranges. The light curve was re-solved after the orbit solution to yield a good fit to the available data, with a flat O−C curve, an rms scatter of 0.021 mag, and $\chi_\nu^2 = 1.64$. The photometric flux ratio of 2.3 is consistent with the spectra. This system is not included in the DIA data base.

3.3.31 8 87175 (DIA 005830.98−723913.8)

Limited spectroscopic data gave seven double-lined spectra in the narrower phase ranges to provide an orbital solution. The well-defined light curve, with deep eclipses, yielded a detached configuration, with a reasonably flat (O−C) curve, an rms scatter of 0.016 mag, and $\chi_\nu^2 = 1.43$, and a flux ratio of 1.1, in agreement with the spectra.

3.3.32 8 104222 (DIA 005825.08−721909.8)

A total of 11 double-lined spectra in the wider phase ranges were available for the orbit solution. The light curve, with deep eclipses

of nearly equal depth, has some inconsistent observations through both eclipses. The best solution, with a reasonably flat (O−C) curve, yields an rms scatter of 0.023 mag, and $\chi_\nu^2 = 2.03$, reflecting the scatter in observations through the eclipses.

3.3.33 8 209964 (DIA 010016.05−721243.9)

The obviously double-lined spectra sampled both quadratures with a total of 14 spectra in the wider phase ranges. The light-curve solution indicates a semidetached configuration and gives a flat (O−C) curve, an rms scatter of 0.009 mag, and $\chi_\nu^2 = 1.38$. The photometric flux ratio of 0.9 is confirmed by the spectra, and again there is a small dip in the observed light curve just before first contact of primary eclipse.

3.3.34 9 10098 (DIA 010052.90−724748.6)

The narrower phase ranges have seven spectra, yielding an orbit solution with a flux ratio greater than unity. The light-curve solution requires a semidetached configuration to match this flux ratio, giving a flat (O−C) curve, an rms scatter of 0.009 mag and $\chi_\nu^2 = 0.74$.

3.3.35 9 47454 (DIA 010052.04−720705.5)

Six spectra observed at both quadratures provide the orbital solution. The light curve appears to be symmetric but the observations have substantial scatter, which is reflected in the rms scatter of 0.016 mag, and $\chi_\nu^2 = 1.94$. The photometric flux ratio of 1.1, confirmed by the spectra, results from a semidetached configuration; a detached solution was also found, but the implied photometric flux ratio of 4.6 is clearly ruled out by the spectra.

3.3.36 9 64498 (DIA 010117.26−724232.1)

A total of 10 spectra in the wider phase ranges was needed to provide an orbital solution. The shallow light curve has an amplitude of only 0.17 mag, but is symmetric. The light-curve solution provides a reasonable fit with a mostly flat (O−C) curve, an rms scatter of 0.011 mag and $\chi_\nu^2 = 0.80$. The photometric flux ratio of 1.8 is consistent with the spectra.

3.3.37 10 37156

Fourteen weakly double-lined spectra in the wider phase ranges were used to find the orbital solution. The spectra show some emission in Hγ, but using only the He I lines gives essentially the same solution. The light curve is quite well defined, but has minimal coverage of the eclipse curves. Initial solutions indicated that secondary eclipse was slightly displaced from phase 0.50, and re-solutions including e, ω yielded a sensible small eccentricity of 0.013. The final solution provides a flat (O−C) curve, with an rms scatter of 0.013 mag and $\chi_\nu^2 = 1.06$, and a flux ratio of 2.9 that is consistent with the spectra.

3.3.38 10 94559

Clearly double-lined spectra with a flux ratio of unity provided an orbital solution from eight observations in the narrower phase ranges. Although the PSF light curve has sparsely defined eclipses, the light-curve solution shows that a semidetached configuration is necessary to provide a photometric flux ratio in agreement with the spectra.

The rms scatter is large, at 0.029 mag, and $\chi_\nu^2 = 3.96$ confirms the limited quality of this star's light curve.

3.3.39 10 108086

Only six double-lined spectra, which indicate a flux ratio near unity, were available in the wider phase ranges to provide an orbital solution. The light curve requires a contact configuration, and was solved by Rucinski's routines for contact binaries incorporated in LIGHT 2, to yield a fill-out factor of $F = 1.70$ (as defined by Mochnacki 1984). A phaseshift of $+0.0040$ was required to improve the model fit, resulting in a flat (O−C) curve, rms scatter of 0.016 mag, and $\chi_\nu^2 = 1.88$. This deep-contact binary, comprising two O stars with masses of 17 and 14 $M_\odot$, has an orbital period of only 0.88 d – a remarkable system.

3.3.40 10 110440

The spectra show emission in the H lines, and the orbital solution (using the spectra in the wider phase ranges) is based only on the He I λ4471 line. The light curve is symmetric and well defined, and the solution yields a flat (O−C) curve with an rms scatter of 0.011 mag and $\chi_\nu^2 = 0.47$ – one of the smallest in the sample. The photometric flux ratio of 1.5 is confirmed by the spectra.

3.3.41 Other systems

Of the remaining ∼60 binaries similarly investigated, many failed to provide meaningful orbital solutions as a result of the specific combinations of observed orbital phases and S/N values achieved in the spectra, as noted in Section 3. Some spectra were significantly contaminated by emission, particularly in the Balmer lines, presumably from nebular sources. At the spectral resolution employed in these fibre-fed spectra, we were unable to remove these nebular lines unambiguously, and hence orbital solutions could not be obtained reliably. None the less, there are evidently several intrinsically interesting binary systems amongst this set, notably 6 89617 and 6 194856, both of which are composed of two O-type stars with orbital periods of, respectively, 0.87 d and 0.65 d. Clearly, such rare objects deserve to be studied more intensively in order to establish their properties and to test models for the formation of close binaries of high mass.

4 ASTROPHYSICAL PARAMETERS AND EVOLUTIONARY CHARACTERISTICS

Astrophysical parameters can be calculated directly from the orbital and light-curve solutions. Results are presented in Table 4 for the components in detached systems, and in Table 5 for the semidetached and contact systems. The 1σ uncertainties on the derived masses, radii, surface gravities, temperatures and luminosities have been calculated by the standard procedures of propagation of uncertainties (errors) from the data given in Tables 1–3 (cf. e.g. Hilditch 2001). For all systems, an uncertainty of ± 1000 K on the mean effective temperature of the primary component was adopted, based on the discussion of the calibration between spectral type and effective temperature given in HHH03.
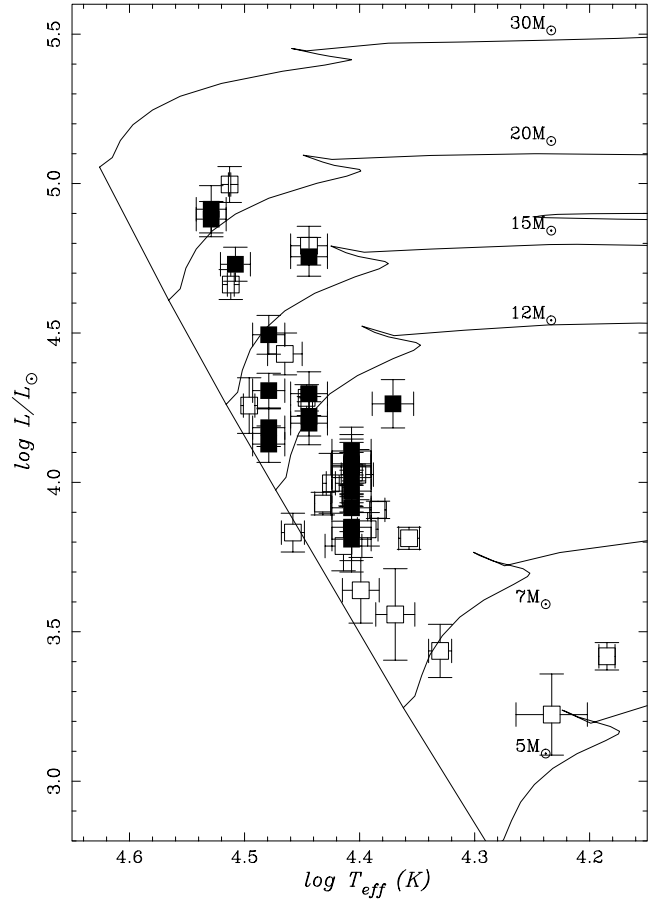
4.1 Detached systems

In any projection of the Hertzsprung–Russell (HR) diagram, the coeval components of a pre-mass-exchange binary must lie on an
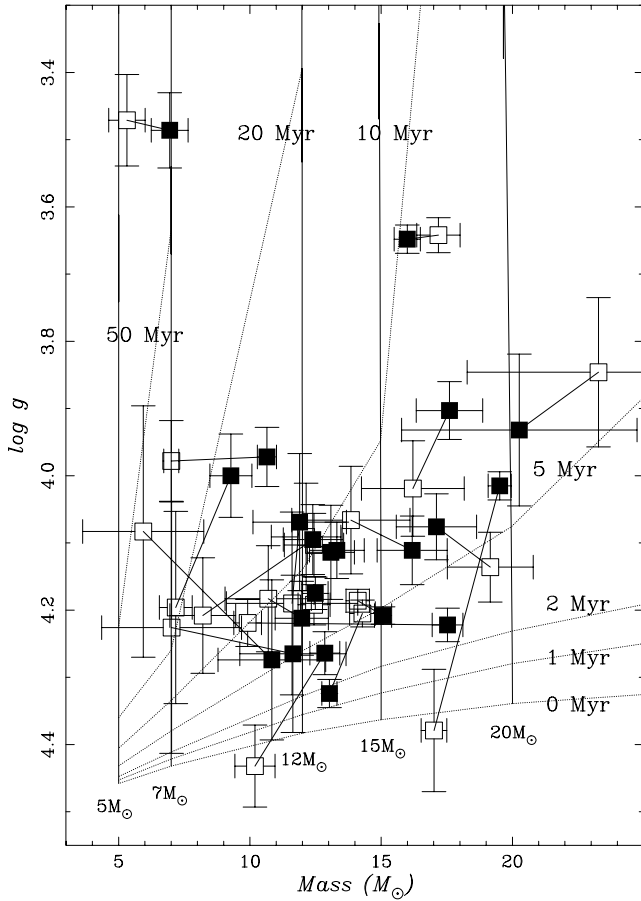
Figure 7. The primary and secondary components (filled and open symbols) of 21 SMC detached binary systems plotted with 1σ uncertainties in the mass–surface gravity plane (18 from this paper, three from HHH03). Lines join the primary and secondary of each binary. Also plotted are evolutionary tracks (solid lines) for single stars of masses 5, 7, 12, 15 and 20 $M_\odot$ and isochrones (dotted lines) for ages of 0, 1, 2, 5, 10 and 20 Myr, taken from the models of Girardi et al. (2000) for $Z = 0.004$, appropriate for the SMC.

Figure 8. The primary and secondary components (filled and open symbols) of 21 SMC detached binary systems plotted with 1σ uncertainties in the $\log T_{\rm eff} - \log (L/L_\odot)$ plane (HR diagram; 18 from this paper, three from HHH03). Also plotted are the zero-age main sequence and evolutionary tracks for single stars of masses 5, 7, 12, 15, 20 and 30 $M_\odot$, taken from the models of Girardi et al. (2000) for $Z = 0.004$, appropriate for the SMC.

isochrone. This expectation is borne out for our sample of SMC detached systems, as illustrated in Fig. 7, where we compare our results for detached systems with the stellar evolution sequences given by Girardi et al. (2000), choosing models for $Z = 0.004$ as appropriate to SMC metallicity, and the mass versus surface gravity plane for the comparison. The average mass ratio for the 21 binaries is 1.2, so that differential evolution due to mass differences is not generally expected to be important. There are a few exceptions, notably 4 103706 (18 + 10 $M_\odot$), 5 255984 (12 + 7 $M_\odot$) and 10 110440 (11 + 6 $M_\odot$), for which the locations of the components are none the less consistent with isochrones to within the 1σ uncertainties.

A second, and more stringent, observational test of the models is to compare the empirical, dynamically determined masses with those inferred from the evolutionary tracks in the HR diagram (Fig. 8). The differences (δM) between the evolutionary mass and the observed mass for each of the 36 stars in detached systems are listed in Table 4, in the sense evolutionary mass minus observed mass. The average difference is $\Delta M = -0.8 \pm 2.1$ $M_\odot$ (s.d.), and, when combined with the six stars in detached systems from HHH03, $\Delta M = -0.9 \pm 2.2$ $M_\odot$ (s.d.). Considering that the

typical uncertainties on the observed masses are $\sim \pm 1$–2 $M_\odot$, this agreement is excellent, and confirms that, where discrepancies occur between 'evolutionary' and 'spectroscopic' masses (e.g. Herrero et al. 1992), it is the spectroscopic results that are more questionable.

A final, straightforward comparison can be made by examining isochrones in the mass–luminosity plane (Fig. 9); all stars should lie above the zero-age main sequence (ZAMS). In practice, most of the observed components are distributed sensibly within their 1σ uncertainties of the expectations from the models. The obvious exceptions are the secondary components of 4 56804, 6 11141 and 10 37156, and the primary component of 4 103706.

The overall conclusion from these comparisons is that agreement is remarkably good between observations and the Girardi et al. (2000) models, with only four exceptions in a sample of 44 stars.

4.2 Semidetached and contact systems

The distribution of the components of the 28 semidetached systems in the mass–surface gravity plane (Fig. 10) could hardly be more different from those of the detached systems. Note that the lines connecting the components of each binary are all at obtuse angles relative to the isochrones, in complete contrast to the detached systems.

Table 4. Astrophysical parameters for detached systems. For each binary the upper/lower rows correspond to the primary/secondary components, respectively.

OGLE-PSF identifier	Mass ($M_\odot$)	Radius ($R_\odot$)	$\log g$ (dex cgs)	$\log T_{eff}$ (dex K)	$\log L$ (dex $L_\odot$)	δM ($M_\odot$)
4 056804	13.0 ± 0.3	4.1 ± 0.1	4.32 ± 0.02	4.479 ± 0.014	4.128 ± 0.061	$+0.2$
	14.3 ± 0.5	4.9 ± 0.1	4.21 ± 0.02	4.384 ± 0.006	3.908 ± 0.029	-4.1
4 103706	17.5 ± 0.6	5.4 ± 0.1	4.22 ± 0.03	4.444 ± 0.016	4.221 ± 0.066	-5.5
	9.9 ± 0.5	4.0 ± 0.1	4.22 ± 0.04	4.432 ± 0.007	3.929 ± 0.038	$+1.0$
4 163552	13.3 ± 1.0	5.3 ± 0.1	4.11 ± 0.04	4.407 ± 0.017	4.062 ± 0.072	-2.7
	12.4 ± 1.1	5.2 ± 0.2	4.10 ± 0.05	4.405 ± 0.003	4.033 ± 0.028	-1.9
5 095194	20.3 ± 4.5	8.1 ± 0.6	3.93 ± 0.11	4.529 ± 0.013	4.914 ± 0.079	$+1.0$
	23.3 ± 5.0	9.5 ± 0.7	3.85 ± 0.11	4.513 ± 0.001	4.997 ± 0.060	-0.8
5 140701	6.9 ± 0.7	7.9 ± 0.3	3.49 ± 0.06	4.371 ± 0.018	4.263 ± 0.081	$+4.3$
	5.3 ± 0.7	7.0 ± 0.3	3.47 ± 0.07	4.185 ± 0.007	3.418 ± 0.046	$+0.4$
5 180064	10.7 ± 0.4	5.6 ± 0.3	3.97 ± 0.04	4.407 ± 0.017	4.105 ± 0.080	$+0.1$
	7.0 ± 0.3	4.5 ± 0.3	3.98 ± 0.06	4.233 ± 0.031	3.223 ± 0.136	-1.5
5 255984	11.6 ± 2.0	4.2 ± 0.4	4.27 ± 0.12	4.407 ± 0.017	3.850 ± 0.112	-1.6
	7.0 ± 2.7	3.4 ± 0.3	4.23 ± 0.19	4.399 ± 0.016	3.639 ± 0.110	$+2.3$
5 305884	17.6 ± 1.3	7.8 ± 0.3	3.90 ± 0.04	4.529 ± 0.013	4.881 ± 0.059	$+3.0$
	16.2 ± 2.0	6.5 ± 0.4	4.02 ± 0.07	4.512 ± 0.003	4.662 ± 0.050	$+1.6$
5 311566	12.8 ± 0.6	4.4 ± 0.1	4.26 ± 0.03	4.479 ± 0.014	4.183 ± 0.063	$+0.5$
	10.2 ± 0.8	3.2 ± 0.2	4.43 ± 0.06	4.458 ± 0.010	3.832 ± 0.065	$+0.9$
6 011141	15.1 ± 0.3	5.1 ± 0.1	4.21 ± 0.01	4.479 ± 0.014	4.307 ± 0.058	-1.3
	14.1 ± 0.4	5.0 ± 0.1	4.19 ± 0.02	4.357 ± 0.009	3.813 ± 0.037	-5.3
6 180084	16.2 ± 1.3	5.9 ± 0.2	4.11 ± 0.05	4.444 ± 0.016	4.297 ± 0.073	-3.5
	13.8 ± 2.3	5.7 ± 0.2	4.07 ± 0.08	4.446 ± 0.005	4.283 ± 0.044	-1.4
6 221543	11.9 ± 1.8	5.3 ± 0.5	4.07 ± 0.10	4.407 ± 0.017	4.056 ± 0.104	-1.3
	11.6 ± 2.5	4.5 ± 0.5	4.19 ± 0.14	4.425 ± 0.004	3.997 ± 0.100	-0.7
7 120044	12.5 ± 0.5	4.8 ± 0.1	4.18 ± 0.02	4.407 ± 0.017	3.971 ± 0.070	-2.0
	12.4 ± 0.6	4.7 ± 0.1	4.19 ± 0.03	4.408 ± 0.007	3.956 ± 0.035	-2.2
7 255621	9.3 ± 0.8	5.0 ± 0.3	4.00 ± 0.06	4.407 ± 0.017	4.016 ± 0.084	$+1.3$
	7.2 ± 0.6	3.5 ± 0.6	4.20 ± 0.14	4.369 ± 0.017	3.558 ± 0.153	$+1.0$
8 087175	12.0 ± 1.0	4.5 ± 0.2	4.21 ± 0.06	4.407 ± 0.017	3.915 ± 0.080	-1.5
	10.7 ± 1.6	4.4 ± 0.2	4.18 ± 0.08	4.393 ± 0.009	3.843 ± 0.056	-0.5
8 104222	13.1 ± 0.9	5.2 ± 0.4	4.11 ± 0.07	4.407 ± 0.017	4.052 ± 0.093	-2.5
	12.1 ± 1.3	5.2 ± 0.4	4.09 ± 0.08	4.402 ± 0.014	4.026 ± 0.084	-1.5
10 037156	19.5 ± 0.4	7.2 ± 0.2	4.02 ± 0.02	4.508 ± 0.013	4.730 ± 0.057	-1.0
	17.0 ± 0.5	4.4 ± 0.5	4.38 ± 0.09	4.496 ± 0.005	4.257 ± 0.093	-2.7
10 110440	10.8 ± 2.1	4.0 ± 0.4	4.27 ± 0.12	4.407 ± 0.017	3.810 ± 0.110	-0.8
	5.9 ± 2.3	3.7 ± 0.3	4.08 ± 0.19	4.330 ± 0.011	3.436 ± 0.089	$+1.0$

In the HR diagram (Fig. 11), the secondary components appear to be systematically older than the primaries *on the basis of single-star models*, and are all much larger than expected for unevolved stars of the same mass. This is a very clear signature that these stars are the mass-losing components seen in the post-rapid-mass-transfer phase of case-A evolution (the longer-lived, slow-mass-transfer phase of case A). In our earlier discussion of orbit and light-curve solutions for individual binaries, it was noted that a substantial number of the semidetached systems displayed clear evidence of small depressions (0.01–0.05 mag) in their light curves occurring just before the onset of primary eclipse. This evidence for absorption by a weak mass-transfer stream (elaborated in Section 3.3.1) occurs in ~40 per cent of our semidetached sample, and may be taken as further evidence of these systems being in the slow phase of mass transfer.

Whilst the locations of the observed secondary components of these semidetached systems in Figs 10 and 11 clearly show that they are evolved mass-losing stars, the observed primary components occupy the main-sequence band. A natural question is whether these stars, which are the mass gainers in case-A evolution, have the observed values of $\log T_{eff}$ and $\log (L/L_\odot)$ that are appropriate for single stars of the same (newly acquired) mass. That is, does the evolutionary mass concur with the observed dynamical mass also for the mass-gaining stars? We have repeated the test carried out for the stars in detached systems on the primary components of the semidetached systems, and the individual differences (δM) are listed in Table 5. The average difference from Table 5 is $\Delta M = -1.0 \pm 4.4\,M_\odot$ (s.d.), which becomes $\Delta M = -0.1 \pm 4.4\,M_\odot$ (s.d.) when the seven primaries in semidetached systems from HHH03 are included.
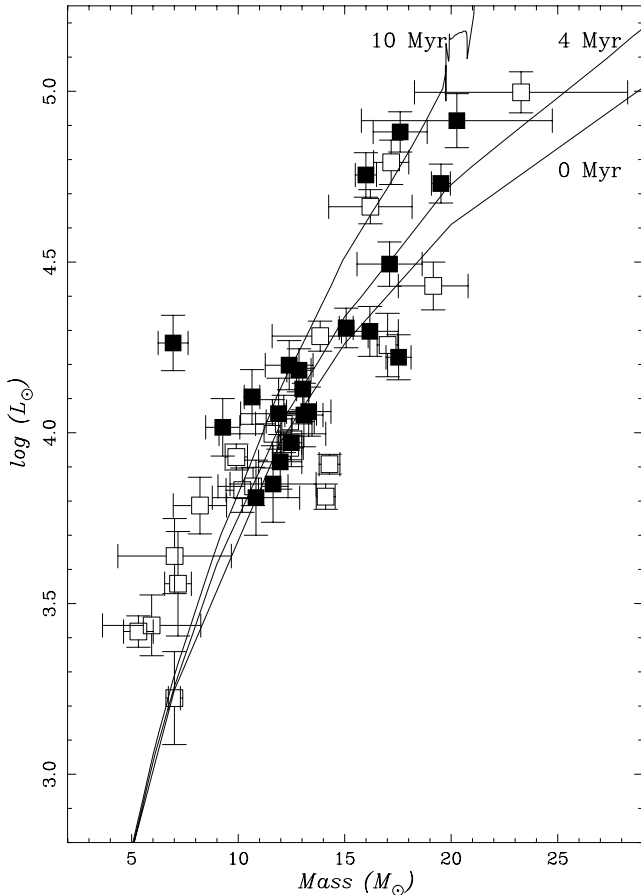
Figure 9. The primary and secondary components (filled and open symbols) of 21 SMC detached binary systems plotted with 1σ uncertainties in the mass–$\log(L/L_{\odot})$ plane (18 from this paper, three from HHH03). Also plotted are isochrones (solid lines) for ages of 0, 4 and 10 Myr from the models of Girardi et al. (2000) for $Z = 0.004$, appropriate for the SMC.

This apparent agreement between evolutionary and observed masses would suggest that the mass gainers do settle into equilibrium states during the slow phase of case A with observed properties appropriate for their newly acquired masses. The examination by Braun & Langer (1995), which also reviewed earlier work on accretion on to massive main-sequence stars, shows that the mass gainers may well adopt such characteristics, provided that their core regions become again well mixed with hydrogen and therefore have 'rejuvenated' cores appropriate for their new total mass. However, mass gainers may not always take that route, but rather develop chemical structures unlike those of single stars, where the core mass remains unchanged from before the mass-transfer process. Such stars would appear to be underluminous for their newly acquired mass. These observational data would suggest that the mass gainers do have rejuvenated cores. However, the dispersion about ΔM is a factor of $\simeq 2$ greater than that for the detached systems, which suggests that the true answer could be more complex.

There are two extreme outliers in the distribution, the primary components of 5 300549 (with $\delta M = -10.4\,M_{\odot}$) and 9 175323 (with $\delta M = +9.6\,M_{\odot}$), and if they are removed from the sample $\Delta M = -0.1 \pm 3.6\,M_{\odot}$ (s.d.). [Systematic errors in observed masses would lead to systematic errors in derived distances, and these two stars are respectively at distance moduli of 18.52 and 18.84, neither of which are unusual for the observed distribution.]

Perhaps the extra dispersion in ΔM is due to some stars not having rejuvenated cores and therefore lower luminosities, but the uncertainties of the data set are not sufficiently small to resolve it. Perhaps one or two of the larger positive δM values could be due to binary systems being observed at the end of the rapid phase of mass transfer where evolution-model luminosities are larger than equilibrium values (Wellstein, Langer & Braun 2001).

These results on SMC semidetached binaries are similar to those for semidetached systems in the Milky Way galaxy (MWG) compiled by Hilditch (2004). For that sample of only 10 systems, the average difference is $\Delta M = +2 \pm 5\,M_{\odot}$, although some of those discrepancies could be due to the adoption of different $T_{\rm eff}$ scales for O-type stars. This type of investigation should be pursued further, with more data of higher quality and on a larger sample, because it could help to resolve the still poorly known efficiency of semiconvective mixing in mass-accreting stars (Wellstein et al. 2001), and whether stellar cores do become rejuvenated in mass-gaining events.

Regrettably, there are no published stellar evolution models for mass-exchanging binary systems in cases A and AB at SMC metallicity ($Z \simeq 0.004$). However, the work of Wellstein & Langer (1999) and Wellstein et al. (2001) for solar-metallicity binaries ($Z = 0.020$) provides many detailed examples of what is expected for the evolution of close binaries with initial orbital periods of a few days and initial masses in our observed range. Examination of their tracks for conservative case-A evolution, followed by case AB at later stages, shows sensible concurrence with well-established semidetached O,B binaries in the MWG, with the observed secondaries identified as the mass-losing original primaries, and the observed primaries as the mass-gaining original secondaries (cf. Hilditch 2004). The models indicate that initial orbital periods of order 2–5 d remain around those values during the early mass-reversal stages and into the slow phase of case A, which is expected to last of the order of 3–5 Myr before the case-AB phase starts (when the orbital periods become much longer).

Our SMC semidetached binaries fit this overall picture well. Our sample is defined by an upper orbital-period limit of $P \lesssim 5$ d, and a faint absolute-magnitude limit of $M_V \simeq -3$, corresponding to a spectral type on the main sequence of about B2. Of our 50 binary systems, 21 are in detached states and 28 are in post-rapid-mass-transfer semidetached states with properties that seem to be consistent with conservative case-A evolutionary models. The durations of the detached phases in the Wellstein & Langer (1999) and Wellstein et al. (2001) models are $\sim$3–12 Myr (dependent on the initial orbital period and masses). The durations of the slow phase of case A are $\sim$1–5 Myr (again dependent on the particular initial conditions). Note that the semidetached phases of evolution for some systems are as long as, or longer than, the detached phases of others.

On the basis of these models, do we therefore expect an observed non-coeval sample to display an approximately $3:4$ division between detached and semidetached systems? Are the particular characteristics of the stars consistent with *conservative* case-A evolution, or is there an overall demand for some mass loss from the binary systems to have occurred during the rapid mass-transfer phase that lasts only some few times 10^4 yr? Binary-star evolutionary models at SMC metallicity are required to compare with observational results on the substantial sample of eclipsing binaries we have presented. The only contact binary in the sample is in deep contact, with a Mochnacki (1984) fill-out factor $F = 1.70$, and will presumably merge into a single star of some $30\,M_{\odot}$. Its origins are unclear, but it is not a unique object amongst SMC or MWG OB binaries.
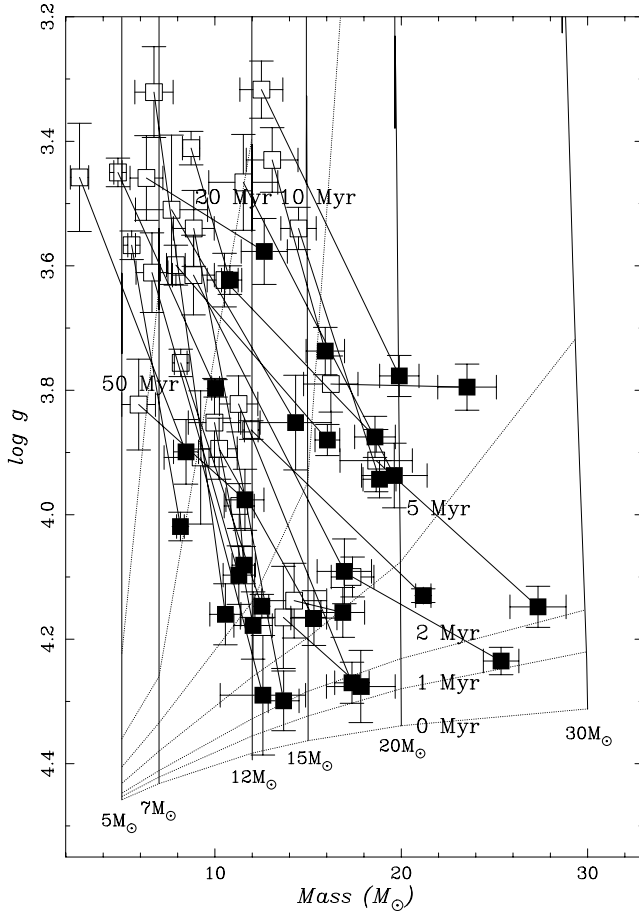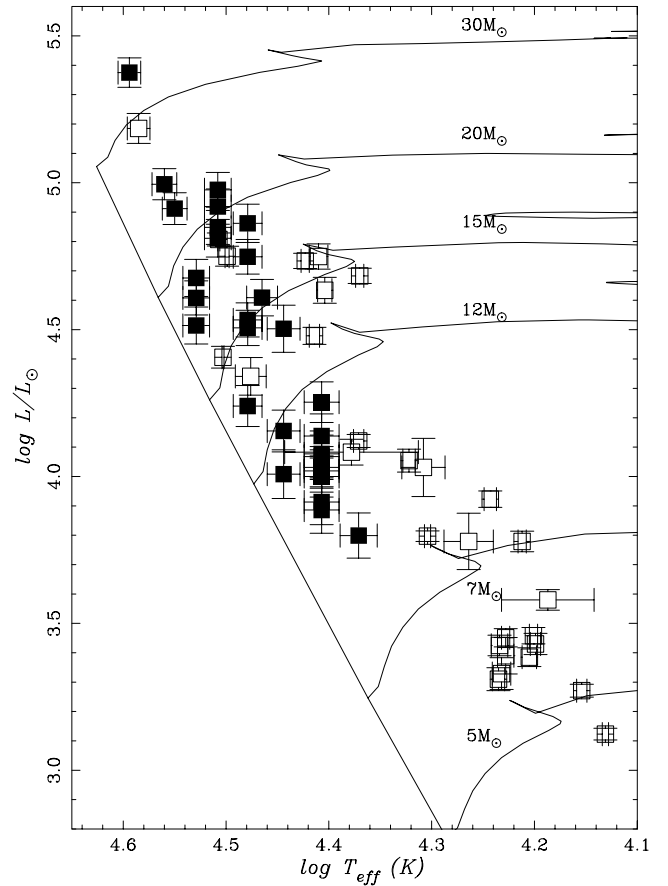
Figure 10. The primary and secondary components (filled and open symbols) of 28 SMC semidetached systems and one SMC contact system plotted with 1σ uncertainties in the mass–surface gravity plane (22 from this paper, seven from HHH03). Lines join the primary and secondary of each system. Also plotted are evolutionary tracks (solid lines) for single stars of masses 5, 7, 12, 15 and 20 $M_\odot$ and isochrones (dotted lines) for ages of 0, 1, 2, 5, 10, 20 and 50 Myr, taken from the models of Girardi et al. (2000) for $Z = 0.004$, appropriate for the SMC.

Figure 11. The primary and secondary components (filled and open symbols) of 28 SMC semidetached systems and one SMC contact system plotted with 1σ uncertainties in the $\log T_{\rm eff} - \log(L/L_\odot)$ plane (HR diagram) (22 from this paper, seven from HHH03). Also plotted are the zero-age main sequence and evolutionary tracks for single stars of masses 5, 7, 12, 15, 20 and 30 $M_\odot$, taken from the models of Girardi et al. (2000) for $Z = 0.004$, appropriate for the SMC.

5 DISTANCES

Our methodology for distance determinations is fully described in HHH03. In brief, the photometric analysis gives the relative sizes of the components in each system, and the spectroscopic orbit puts these dimensions on an absolute scale. An effective temperature is assigned to the primary on the basis of its spectral type; its absolute magnitude then follows from a light-curve synthesis code that utilizes surface brightnesses from line-blanketed model atmospheres (we use those given by Howarth & Lynas-Gray 1989). The light-curve solution gives the relative brightnesses of the components, and hence the absolute magnitude of the system. The true distance modulus is determined using *I*-band data, as the reddening is smaller, and the intrinsic fluxes less temperature-sensitive, at longer wavelengths; extinction is determined from $(B - I)$ colours.

Because many of our stars are somewhat cooler than the (predominantly O-type) targets of HHH03, a single 'hot star' colour is no longer adequate; instead we adopted intrinsic colours from an approximate fit to model results,

$$(B - I)_0 = \max\{-0.6, 2.97 - 0.78 \log[T_{\rm eff}(1)]\} \qquad 5$$

[for $\log(T_{\rm eff}) \gtrsim 4.3$]. In a handful of cases this leads to values for $A(I)$ that are smaller than the expected foreground value of $\sim$0.09 [$E(B - V) \simeq 0.05$]; we none the less retain the computed values in order not to bias the mean distance modulus.

Results are summarized in Table 6. The mean true distance modulus (DM) for this sample is 18.88 ± 0.30 (s.d.), ranging from 18.29 to 19.48, and the mean extinction is $A(I) = 0.179 \pm 0.070$ [$E(B - V) = A(I)/1.8 = 0.099 \pm 0.040$]. The mean DM may be compared with the value of 18.89 ± 0.14 (range 18.71–19.13) obtained from 10 stars by HHH03.

In the present sample, there is no correlation of DM with $A(I)$, $m(I)$, or γ velocity, but there *is* a modest correlation with $M(I)$ (Pearson and Spearman correlation coefficients indicating that the null hypothesis of no correlation can be rejected with $\sim$99.5 per cent confidence). Fig. 12 shows that this correlation arises from a simple selection effect: the sample omits intrinsically faint systems with large derived DM, simply because such systems are excluded by our apparent-magnitude cut-off. This biases the mean DM towards a too-small value. Restricting the sample to $M(I)$ brighter than -3.0 removes any correlation and gives a mean DM of 18.967 ± 0.311 from 29 stars, which we adopt as the best estimate from the present sample.

Table 5. Astrophysical parameters for semidetached and contact systems. For each binary the upper/lower rows correspond to the primary/secondary components, respectively.

| OGLE-PSF identifier	Mass (M$_\odot$)	Radius (R$_\odot$)	log g (dex cgs)	log $T_{\rm eff}$ (dex K)	log L (dex L$_\odot$)	δM (M$_\odot$)
1 099121	11.3 ± 0.8	5.0 ± 0.2	4.10 ± 0.05	4.444 ± 0.015	4.155 ± 0.071	+0.5
	6.6 ± 0.9	6.7 ± 0.2	3.61 ± 0.06	4.199 ± 0.005	3.430 ± 0.036	
4 110409	13.7 ± 0.8	4.3 ± 0.2	4.30 ± 0.05	4.407 ± 0.017	3.886 ± 0.079	−5.6
	8.9 ± 1.1	8.4 ± 0.3	3.54 ± 0.06	4.187 ± 0.045	3.580 ± 0.035	
5 026631	11.5 ± 0.6	5.1 ± 0.1	4.08 ± 0.03	4.407 ± 0.017	4.031 ± 0.071	−0.9
	11.3 ± 0.8	5.7 ± 0.1	3.99 ± 0.04	4.234 ± 0.008	3.425 ± 0.035	
5 060548	10.8 ± 0.4	8.4 ± 0.1	3.62 ± 0.02	4.479 ± 0.014	4.748 ± 0.059	+6.7
	8.7 ± 0.4	9.6 ± 0.2	3.41 ± 0.03	4.243 ± 0.006	3.923 ± 0.028	
5 208049	10.0 ± 0.2	6.6 ± 0.1	3.80 ± 0.01	4.407 ± 0.017	4.253 ± 0.069	+1.5
	4.8 ± 0.2	6.8 ± 0.1	3.45 ± 0.02	4.154 ± 0.005	3.271 ± 0.022	
5 243188	27.3 ± 1.5	7.3 ± 0.2	4.15 ± 0.03	4.550 ± 0.012	4.912 ± 0.054	−4.7
	18.7 ± 1.9	7.9 ± 0.2	3.91 ± 0.05	4.507 ± 0.001	4.807 ± 0.022	
5 277080	17.4 ± 0.9	5.0 ± 0.1	4.27 ± 0.03	4.407 ± 0.017	4.019 ± 0.072	−6.9
	11.3 ± 1.0	6.8 ± 0.2	3.82 ± 0.05	4.201 ± 0.004	3.458 ± 0.028	
5 300549	25.4 ± 1.0	6.4 ± 0.1	4.24 ± 0.02	4.479 ± 0.014	4.506 ± 0.060	−10.4
	17.4 ± 1.1	6.1 ± 0.1	4.10 ± 0.03	4.205 ± 0.007	3.385 ± 0.032	
6 152981	12.5 ± 0.4	4.9 ± 0.1	4.15 ± 0.02	4.407 ± 0.017	4.000 ± 0.070	−2.0
	8.2 ± 0.3	6.3 ± 0.1	3.76 ± 0.02	4.304 ± 0.003	3.797 ± 0.018	
6 251047	8.1 ± 0.2	4.6 ± 0.1	4.02 ± 0.02	4.371 ± 0.018	3.799 ± 0.077	+0.9
	5.5 ± 0.2	6.4 ± 0.1	3.57 ± 0.02	4.131 ± 0.003	3.123 ± 0.020	
6 311225	21.2 ± 0.4	6.6 ± 0.1	4.13 ± 0.01	4.479 ± 0.014	4.533 ± 0.058	−6.2
	11.9 ± 0.4	6.7 ± 0.1	3.86 ± 0.02	4.371 ± 0.005	4.121 ± 0.022	
6 319960	10.6 ± 0.8	4.5 ± 0.2	4.16 ± 0.05	4.407 ± 0.017	3.913 ± 0.077	−2.4
	6.7 ± 1.0	9.4 ± 0.3	3.32 ± 0.07	4.212 ± 0.004	3.779 ± 0.035	
7 066175	19.6 ± 1.8	7.9 ± 0.3	3.94 ± 0.05	4.508 ± 0.013	4.811 ± 0.064	−0.5
	11.5 ± 1.9	10.4 ± 0.4	3.47 ± 0.08	4.404 ± 0.007	4.634 ± 0.044	
7 142073	12.6 ± 1.2	9.6 ± 0.3	3.58 ± 0.05	4.479 ± 0.014	4.862 ± 0.065	+6.2
	6.3 ± 0.9	7.8 ± 0.3	3.46 ± 0.07	4.322 ± 0.006	4.054 ± 0.039	
7 189660	15.3 ± 1.2	5.3 ± 0.2	4.17 ± 0.04	4.407 ± 0.017	4.068 ± 0.073	−4.9
	10.2 ± 1.0	6.0 ± 0.2	3.89 ± 0.05	4.228 ± 0.004	3.451 ± 0.031	
7 193779	11.6 ± 1.0	5.8 ± 0.2	3.98 ± 0.05	4.407 ± 0.017	4.138 ± 0.075	−0.6
	5.9 ± 0.9	4.9 ± 0.2	3.82 ± 0.07	4.235 ± 0.006	3.310 ± 0.039	
8 209964	18.8 ± 0.9	7.7 ± 0.2	3.94 ± 0.03	4.560 ± 0.012	4.995 ± 0.053	+5.8
	14.5 ± 1.0	10.7 ± 0.2	3.54 ± 0.03	4.423 ± 0.004	4.734 ± 0.026	
9 010098	17.8 ± 1.8	5.1 ± 0.2	4.28 ± 0.06	4.529 ± 0.013	4.514 ± 0.063	0.0
	13.7 ± 2.3	5.1 ± 0.2	4.17 ± 0.08	4.503 ± 0.001	4.406 ± 0.037	
9 047454	12.6 ± 2.3	4.2 ± 0.3	4.29 ± 0.10	4.444 ± 0.016	4.008 ± 0.083	−1.2
	9.2 ± 2.0	5.6 ± 0.3	3.91 ± 0.11	4.228 ± 0.008	3.390 ± 0.062	
9 064498	8.4 ± 0.7	5.4 ± 0.2	3.90 ± 0.05	4.407 ± 0.017	4.077 ± 0.078	+2.3
	2.7 ± 0.5	5.1 ± 0.2	3.46 ± 0.09	4.232 ± 0.009	3.329 ± 0.054	
10 094559	12.0 ± 1.0	4.7 ± 0.2	4.18 ± 0.05	4.479 ± 0.014	4.240 ± 0.070	+1.4
	10.0 ± 1.4	6.2 ± 0.3	3.85 ± 0.07	4.378 ± 0.065	4.083 ± 0.044	
10 108086	16.9 ± 1.2	5.7 ± 0.2	4.16 ± 0.04	4.529 ± 0.013	4.608 ± 0.058	
	14.3 ± 1.7	5.3 ± 0.2	4.14 ± 0.06	4.476 ± 0.015	4.341 ± 0.064	

Our results also show no statistically significant correlation of DM with celestial coordinates. However, Groenewegen (2000) has recently analysed the intrinsic structure of the Magellanic Clouds, using Cepheid photometry and adopting a simple triaxial model. For the SMC, he finds a ∼2 kpc variation in mean distance (∼0.07 in DM) over the ∼2° spatial extent of our sample. Our results are

consistent with this, a linear fit of distance along the projected 'axis' of the SMC suggesting that the north-east extreme is ∼0.1 mag closer than the south-west.

Groenewegen also discusses the line-of-sight depth of the SMC, finding an rms depth of 0.11 mag (3 kpc) for Cepheids. While the distance moduli from HHH03 and the present sample are both

Table 6. Distance determinations. $M(I)$ and I_0 are the absolute and observed I-band quadrature magnitudes, and DM is the true (reddening-free) distance modulus. The I-band extinction $A(I)$ is discussed in Section 5.

OGLE	$M(I)$	I_0	$A(I)$	DM	OGLE	$M(I)$	I_0	$A(I)$	DM
01 099121	−3.16	16.30	0.17	19.29	06 221543	−3.61	15.70	0.21	19.09
04 056804	−3.22	15.77	0.33	18.66	06 251047	−2.93	15.97	0.21	18.69
04 103706	−3.12	15.85	0.31	18.65	06 311225	−3.47	15.20	0.14	18.52
04 110409	−2.90	15.87	0.36	18.40	06 319960	−3.08	16.09	0.11	19.05
04 163552	−3.14	15.41	0.06	18.49	07 066175	−4.65	14.46	0.33	18.77
05 026631	−2.94	15.99	0.14	18.79	07 120044	−3.01	15.81	0.10	18.72
05 060548	−3.57	15.86	0.21	19.22	07 142073	−2.76	16.20	0.14	18.82
05 095194	−3.20	16.23	0.14	19.29	07 189660	−4.51	15.06	0.19	19.38
05 140701	−3.63	15.24	0.25	18.62	07 193779	−3.27	16.19	0.19	19.27
05 180064	−3.13	16.11	0.19	19.05	07 255621	−3.09	16.13	0.27	18.95
05 208049	−4.65	14.98	0.15	19.48	08 087175	−3.21	16.04	0.14	19.10
05 243188	−4.92	14.64	0.23	19.33	08 104222	−4.81	14.56	0.24	19.13
05 255984	−2.51	16.24	0.20	18.54	08 209964	−2.55	16.24	0.17	18.62
05 277080	−3.13	16.07	0.25	18.95	09 010098	−3.70	15.59	0.11	19.18
05 300549	−4.49	14.16	0.14	18.52	09 047454	−3.01	16.26	0.15	19.12
05 305884	−4.39	14.65	0.18	18.86	09 064498	−2.84	16.03	0.12	18.75
05 311566	−2.82	16.03	0.19	18.66	10 037156	−3.76	15.49	0.14	19.11
06 011141	−3.87	15.48	0.15	19.20	10 094559	−2.40	16.32	0.07	18.64
06 152981	−2.93	15.76	0.05	18.64	10 108086	−3.41	15.43	0.08	18.76
06 180084	−2.79	16.17	0.18	18.78	10 110440	−3.43	15.03	0.16	18.29
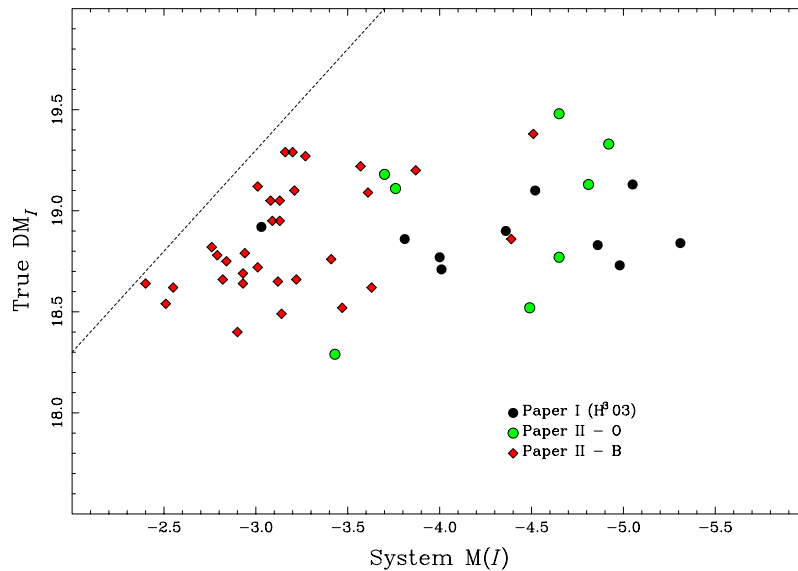
Figure 12. Distance moduli as a function of absolute magnitude (I band). O- and B-type stars are identified, as are results from HHH03. The diagonal line roughly corresponds to the magnitude cut-off in our sample, and illustrates a modest selection bias.

consistent with a single mean value, the present sample has a significantly larger dispersion (with 95 per cent confidence). If the dispersion in the HHH03 sample (for which internal and external error estimates were in close agreement) were representative of the stochastic errors in the present sample, then the residual dispersion of ∼0.28 m (∼8 kpc) in the present sample would reflect astrophysical effects. However, this is surely a substantial overestimate of the true dispersion in our parent population, given the significantly larger observational uncertainties in the current data set. We consider that our results are therefore again consistent with the Cepheid studies in this respect.

Taking the weighted mean of the two eclipsing binary samples (HHH03 and the present paper), our best estimate of the true distance modulus to the SMC is 18.912 ± 0.035 (60.6 ± 1.0 kpc), where the quoted s.e. is, of course, an *internal* error; the result is subject to systematic uncertainties at the ∼0.1 mag level, as discussed in detail by HHH03.

Much work on the extragalactic distance scale is tied to the Large Magellanic Cloud (LMC) distance modulus (e.g. the *HST* Hubble Constant Key Project; Freedman et al. 2001), because the structure of that galaxy has historically been regarded as better understood than that of the SMC. We intend to address LMC binaries directly

in future work, but the difference in distance moduli, SMC−LMC, is quite well documented as +0.5 mag (e.g. Udalski et al. 1999; Groenewegen 2000). Our SMC results therefore imply an LMC DM of 18.41 ± 0.04 ± 0.1, as compared with a value of 18.50 adopted in the Key Project work, and hence a revision of H_0 from 72 to 75 km s^{-1} Mpc^{-1}.

6 CONCLUSION

Together with results from HHH03, our sample of SMC binaries includes 50 systems. With only two or three obvious exceptions, the typical uncertainties are ±10 per cent on masses, ±4 per cent on radii, and ±0.07 on $\log L$ – remarkably good values considering the limited spectral resolution and data quality available for this study, and the use only of single-passband light curves. For comparison, in a recent review of the observed properties of high-mass eclipsing binaries, Hilditch (2004) adopted similar upper limits for the uncertainties on these quantities derived for Galactic O,B binaries, and found only 22 systems that satisfied these criteria. The aims of this project have thus clearly been realized, in that we have provided good determinations of fundamental parameters for the largest sample of O,B type eclipsing binaries achieved for any galaxy (including the Milky Way), and have made a direct determination of the SMC distance modulus that has exceptionally high precision (and very good accuracy). We find good agreement between our observations and the evolutionary models, with no evidence for a 'mass discrepancy' in the models.

REFERENCES

Braun H., Langer N., 1995, A&A, 297, 483
Clausen J. V., Storm J., Larsen S. S., Giménez A., 2003, A&A, 402, 509
Evans C. J., Howarth I. D., Irwin M. J., Burnley A. W., Harries T. J., 2004, MNRAS, 353, 601
Freedman W. L. et al., 2001, ApJ, 553, 47
Girardi L., Bressan A., Bertelli G., Chiosi C., 2000, A&AS, 141, 371
Graczyk D., 2003, MNRAS, 342, 1334
Groenewegen M. A. T., 2000, A&A, 363, 901
Hadrava P., 2004, in Hilditch R. W., Hensberge H., Pavlovski K., eds, ASP Conf. Ser. Vol. 318, Spectroscopically and Spatially Resolving the Components of Close Binary Stars. Astron. Soc. Pac., San Francisco, p. 86
Harries T. J., Hilditch R. W., Howarth I. D., 2003, MNRAS, 339, 157 (HHH03)
Herrero A., Kudritski R. P., Vilchez J. M., Kunze D., Butler K., Haser S., 1992, A&A, 261, 209
Hilditch R. W., 2001, An Introduction to Close Binary Stars. Cambridge Univ. Press, Cambridge, p. 279 et seq
Hilditch R. W., 2004, in Hilditch R. W., Hensberge H., Pavlovski K., eds, ASP Conf. Ser. Vol. 318, Spectroscopically and Spatially Resolving the Components of Close Binary Stars. Astron. Soc. Pac., San Francisco, p. 198
Hill G., 1979, Publ. Dom. Astrophys. Obs., 15, 297
Hill G., 1982, Publ. Dom. Astrophys. Obs., 16, 59
Hill G., Hutchings J. B., 1971, ApJ, 167, 137
Hill G., Rucinski S. M., 1993, in Milone E. F., ed., Light Curve Modelling of Eclipsing Binary Stars. Springer, New York, p. 135
Holmgren D., 2004, in Hilditch R. W., Hensberge H., Pavlovski K., eds, ASP Conf. Ser. Vol. 318, Spectroscopically and Spatially Resolving the Components of Close Binary Stars. Astron. Soc. Pac., San Francisco, p. 95
Howarth I. D., Lynas-Gray A. E., 1989, MNRAS, 240, 513
Ilijic S., 2004, in Hilditch R. W., Hensberge H., Pavlovski K., eds, ASP Conf. Ser. Vol. 318, Spectroscopically and Spatially Resolving the Components of Close Binary Stars. Astron. Soc. Pac., San Francisco, p. 107
Lennon D. J., 1997, A&A, 317, 871
Lewis I. J. et al., 2002, MNRAS, 333, 279
Mochnacki S. W., 1984, ApJS, 55, 551
Ribas I., Giménez A., eds, 2004, New Astron. Rev., 48, 647
Simon K. P., Sturm E., 1994, A&A, 291, 286
Udalski A., Soszyński I., Szymański M., Kubiak M., Pietrzyński G., Woźniak P., Żebruń K., 1998, Acta Astron., 48, 563
Udalski A., Szymański M., Kubiak M., Pietrzyński G., Soszyński I., Woźniak P., Żebruń K., 1999, Acta Astron., 49, 201
Walborn N. R., Fitzpatrick E. L., 1990, PASP, 102, 379
Wellstein S., Langer N., 1999, A&A, 350, 148
Wellstein S., Langer N., Braun H., 2001, A&A, 369, 939
Wyithe J. S. B., Wilson R. E., 2001, ApJ, 559, 260
Wyithe J. S. B., Wilson R. E., 2002, ApJ, 571, 293
Wyrzykowski L. et al., 2004, Acta Astron., 54, 1
Zebrun K. et al., 2001, Acta Astron., 51, 317

This paper has been typeset from a TEX/LATEX file prepared by the author.